Lee *et al. Journal of Nanobiotechnology* (2026) 24:233
https://doi.org/10.1186/s12951-025-03938-2

Journal of Nanobiotechnology

RESEARCH

Open Access

Electrically stimulated asymmetric double-layer scaffolds using 3D printing and electrospinning for enhanced bacteria-free wound healing application

Jieun Lee[1,2†], Aayushi Randhawa[1,2†], Hyeonseo Park[1,2], Hojin Kim[1,2], Seong-Jun Cho[3*] and Ki-Taek Lim[1,2*]

Abstract
Wound healing is a complex process that can be severely impaired in chronic or infected wounds. To overcome these challenges, we developed a bioinspired, double-layer asymmetric hydrogel scaffold combining a conductive hydrogel with an antibacterial electrospun fiber layer. The conductive hydrogel, composed of gelatin, Poly(3,4-ethylenedioxythiophene)-poly(styrenesulfonate) (PEDOT: PSS), and carboxymethyl chitosan (CMCS), provides electrical conductivity under external electric fields, thereby promoting cell activity, migration, and tissue regeneration. CMCS further contributes antibacterial and hydrating properties, creating a favorable microenvironment for wound repair. The electrospun fiber layer, consisting of polycaprolactone (PCL), polylactic acid (PLA), and curcumin (CUR), provides sustained antibacterial protection by inhibiting bacterial proliferation and forming a protective barrier. In vitro experiments showed that electrical stimulation (ES) enhanced cell migration and alignment via electrotaxis, while the electrospun fiber layer effectively suppressed bacterial growth. These results demonstrate the synergistic effect of the conductive hydrogel and antibacterial electrospun fiber layer. This multifunctional, skin-like dressing addresses limitations in current wound care by integrating electrical stimulation with bioactive materials, accelerating tissue regeneration, and providing long-term antibacterial efficacy. The scaffold design mimics natural skin properties and supports efficient wound healing, highlighting its potential as a platform for regenerative medicine applications.

Keywords Electrical stimulation (ES), Conductive hydrogel, Antibacterial electrospun fibers, Wound healing, 3D printing

---

[†] Jieun Lee and Aayushi Randhawa contributed equally to this manuscript.

*Correspondence:
Seong-Jun Cho
sj.cho@kangwon.ac.kr
Ki-Taek Lim
ktlim@kangwon.ac.kr

Full list of author information is available at the end of the article

Graphical Abstract

Graphical illustration of the present study. Showing the fabrication of a double layered structure with antibacterial and wound healing abilities.

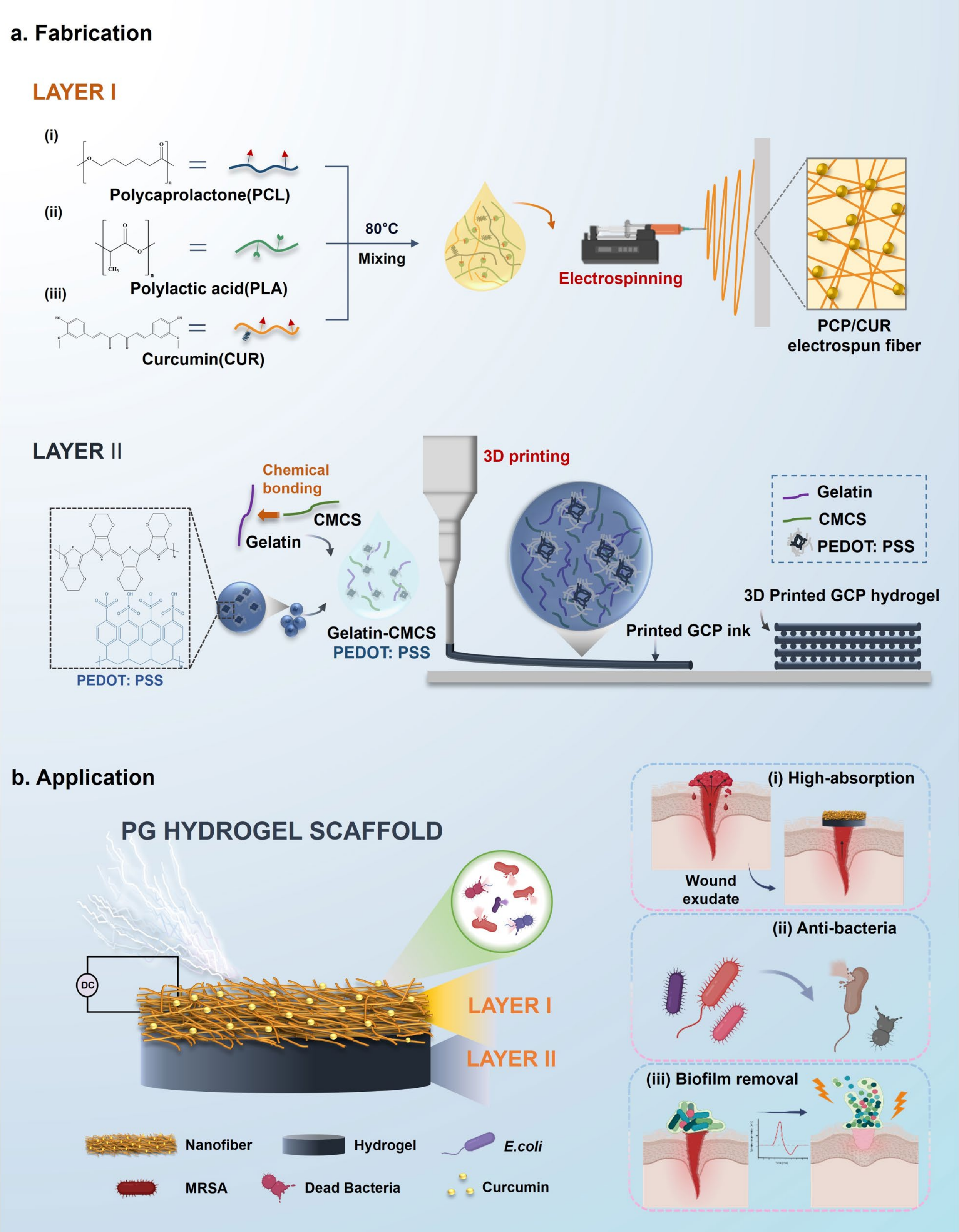

Introduction

Wound healing is a complex physiological process involving cell migration, proliferation, differentiation, and remodeling to restore damaged tissues [1, 2]. However, chronic wounds, such as diabetic ulcers, burns, trauma, or infected wounds, can disrupt this process, impeding cellular activities and tissue regeneration [3, 4]. Traditional wound dressings often fail to create an optimal healing environment, particularly in non-healing wounds [5]. As a result, there is a growing demand for innovative therapeutic strategies that can regulate the wound environment and accelerate the healing process [6–8]. Recent studies have shown that physical stimuli, such as electrical stimulation (ES), effectively promote wound healing, and there has been significant progress in developing conductive biomaterials to harness this potential [9–12]. To address these challenges, researchers have increasingly turned to biomimetic approaches, which aim to replicate the structure and function of natural skin. These strategies seek to create wound healing environments that closely mimic the physiological conditions of healthy skin, promoting more effective and natural healing processes.

ES is vital for enhancing tissue regeneration by inducing key cellular behaviors, such as electrotaxis (directed cell migration), proliferation, and differentiation [13]. In normal tissues, electrical signals are naturally present but may weaken or disappear following severe injuries [14]. ES restores these signals by providing appropriate voltage and frequency, thereby modulating cellular responses and promoting healing [15]. Specifically, ES enhances the migration and proliferation of fibroblasts and keratinocytes, facilitating new tissue formation at the wound site [16–19]. Direct current (DC) ES at 250 mV for 20 min/day has been reported to significantly enhance the proliferation of human bone marrow-derived mesenchymal stem cells (hBMSCs) [20]. Accordingly, the ES parameters in this study were optimized to 200 mV for 25 min/day to ensure effective stimulation while minimizing potential thermal and electrochemical effects.

Furthermore, it stimulates angiogenesis and extracellular matrix (ECM) formation, optimizing the wound environment for recovery [21–23]. Additionally, ES generates reactive oxygen species (ROS) and hydrogen peroxide (H_2O_2), which are critical for inhibiting bacterial growth and disrupting biofilm structures. These molecules damage bacterial cell membranes, proteins, and DNA, leading to bacterial death and the suppression of biofilms. ROS-induced oxidative stress degrades key bacterial components, while H_2O_2 penetrates cell membranes and converts them into ROS, further enhancing antibacterial effects.

Although the use of electrospun fiber membranes to provide antibacterial properties and conductive polymers to promote cell activity have been investigated in earlier research, these approaches are frequently constrained by their low biocompatibility, limited integration, and inability to replicate the layered structure of natural skin [24–26]. To overcome these restrictions, we developed the PG hydrogel scaffold. This structurally biomimetic double-layer scaffold combines a top layer of PCP/CUR (PCL + PLA + CUR) electrospun fibers and a base layer of GCP (gelatin + CMCS + PEDOT: PSS) hydrogel, designed to mimic the key features of the epidermis and dermis, respectively [27, 28].

Importantly, the morphological parameters of each layer were carefully tuned to resemble the hierarchical architecture of natural skin. The electrospun PCP/CUR electrospun fiber layer exhibited an average fiber diameter ranging from 33.66 to 5.30 μm, which corresponds to the microscale collagen bundles and keratin filament network found in the epidermal ECM. Meanwhile, the 3D-printed GCP hydrogel exhibited tunable pore sizes ranging from approximately 201.94 μm to 64.94 μm, depending on the PEDOT: PSS concentration, closely matching the porous architecture of dermal connective tissue (20–125 μm pore size) [29]. This multiscale structural correspondence provides an ECM-like topography that can promote fibroblast infiltration, nutrient diffusion, and neovascularization. At the same time, the 0°/90° printing pattern further emulates the anisotropic alignment characteristic of dermal collagen fibers. Such morphological biomimicry allows the PG hydrogel scaffold to bridge the structural and functional gap between synthetic materials and native skin tissue, offering a biologically relevant platform for wound repair.

This study aims to evaluate the effects of ES on the wound healing process, facilitated by the PG hydrogel, by combining spatial biomimicry, electroconductivity, and structural layering into a structure that dynamically supports key stages of wound healing (Figure 1). This approach enables synchronized promotion of bacterial infection control and tissue regeneration. Thereby providing innovative solutions for the effective management of chronic wounds and facilitating more natural healing processes.

Experimental sections

Materials

N, N-dimethylformamide (DMF) and dichloromethane (DCM) were purchased from Shanghai Titan Scientific Co., Ltd., China. The polycaprolactone (PCL) (Mw: 80,000), poly(lactic acid) (PLA) from a 3D factory (Republic of Korea), and CUR were purchased from Sigma-Aldrich (USA). The high-molecular-weight chitosan powder (Mw: 310–375 kDa, deacetylated chitin: >75%) was also obtained from Sigma-Aldrich, USA. Sodium hydroxide was sourced from Junsei Chemicals,

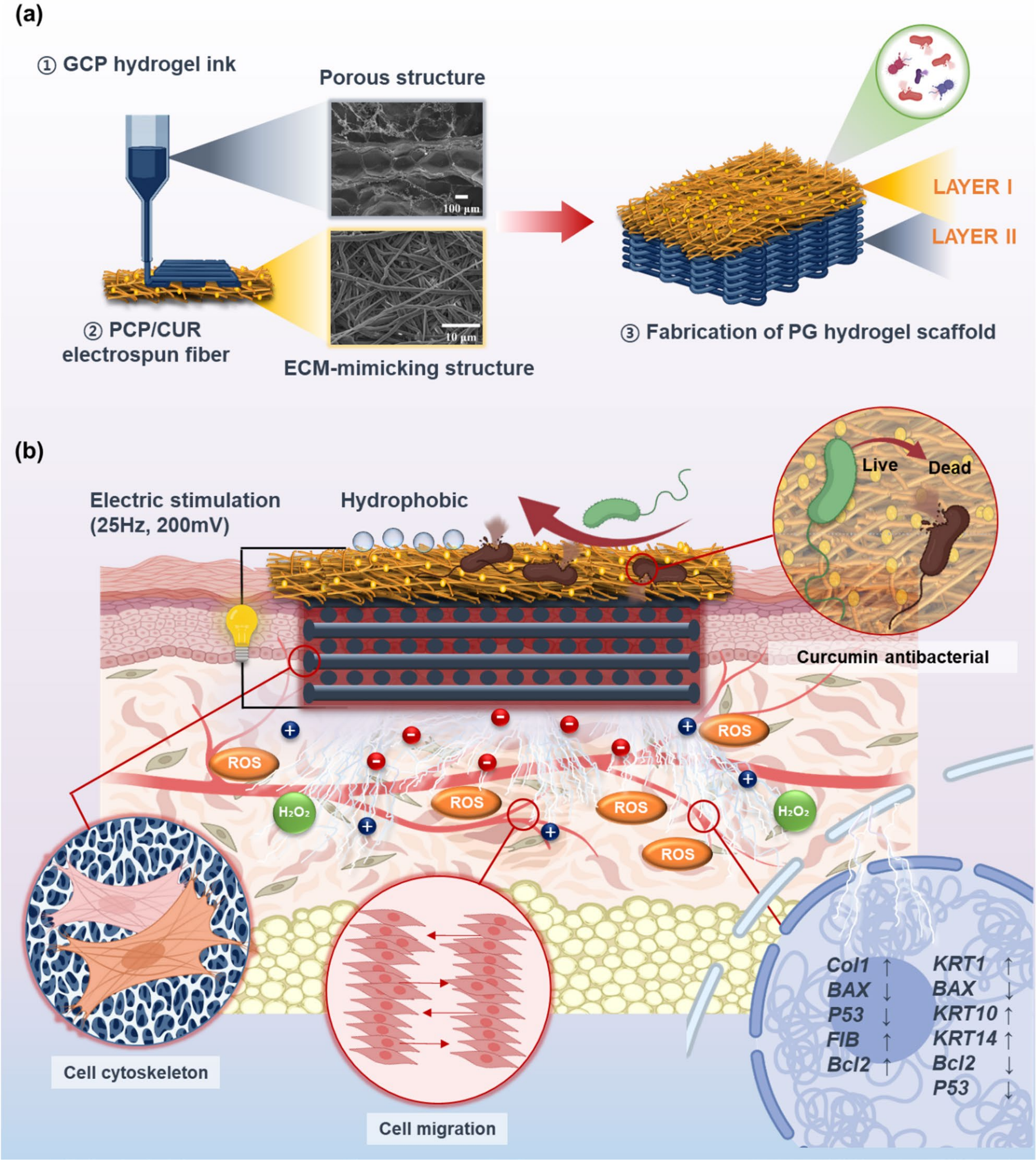

Fig. 1 (**a**) Schematic illustration of the double layered PG hydrogel scaffold, consisting of a electrospun fiber top layer and a hydrogel bottom layer. **(b)** Mechanistic illustration showing how the PG hydrogel scaffold promotes cell migration and exhibits antibacterial activity to enhance wound healing.

Japan. Isopropanol and glutaraldehyde (50% wt, certified) were obtained from Thermo Fisher Scientific, USA. Gelatin type B powder from porcine skin (purity: ≥ 98%; gel strength appx. 300 g bloom) and PEDOT: PSS were purchased from Sigma-Aldrich (USA). All other chemicals and reagents used were of analytical grade. A fully automated CELLINK® BIO-X 3D bio-printer was purchased from CELLINK Corporation, Sweden. Biomechangen Ltd., Republic of Korea, supplied a custom-designed microcurrent stimulation device. *Escherichia coli* (*E.coli*) was provided from the Korean Collection of Type Cultures (KCTC) (Jeonbuk, Republic of Korea).

Table 1 Concentration of PCL, PLA, and CUR complex in electrospun fiber development

Compositions	PCL (w/v)	PLA (w/v)	CUR (w/v)	Total Volume
PC	1.8 g	0 g	0 g	10 ml
PCP	1.2 g	0.072 g	0 g	10 ml
PCP/CUR-1	1.2 g	0.072 g	0.013 g	10 ml
PCP/CUR-3	1.2 g	0.072 g	0.054 g	10 ml

Table 2 Concentration of Gelatin, CMCS, PEDOT: PSS complex in hydrogel development

Compositions	Gelatin (w/v)	CMCS (w/v)	PEDOT: PSS (v/v)	D.I	Total Volume
GCP_0	0.8 g	0.2 g	0 mL	10 mL	10 mL
$GCP_{0.25}$	0.8 g	0.2 g	0.25 mL	9.75 mL	10 mL
$GCP_{0.5}$	0.8 g	0.2 g	0.5 mL	9.5 mL	10 mL
GCP_1	0.8 g	0.2 g	1 mL	9 mL	10 mL
GCP_2	0.8 g	0.2 g	2 mL	8 mL	10 mL

DifcoM Tryptic Soy Broth and BBLM Mannitol Salt Agar were purchased from Becton. WST-8 kit (Cellrix®, Medi-Fab Co., Ltd., Seoul, and Republic of Korea), human dermal fibroblasts (HDF, ATCC No. PCS-201-012), human keratinocyte (HaCaT, ATCC No. PCS-200-011>), and Methicillin-resistant *Staphylococcus aureus* (MRSA, ATCC BAA-41) were purchased from American Type Cell Culture (ATCC) (Manassas, Virginia, USA). The Live-dead staining kit and F-actin probe were purchased from Sigma-Aldrich, USA. Crystal violet was purchased from the Tokyo Chemical Industry (Tokyo, Japan). The WST-8 kits (Cellrix®) were provided by MediFab Co., Ltd. (Seoul, Republic of Korea). The PrimerScript™ RT kit and SYBR Green qRT-PCR master mix were obtained from TaKaRa Bioscience (Japan). Western blot antibodies and cell culture reagents were sourced from Welgene (Republic of Korea) and Santa Cruz Biotechnology (USA).

Preparation of PCP/CUR electrospun fiber and conductive GCP hydrogel

For electrospun fiber synthesis, a blend solution was prepared by dissolving 12% poly(ε-caprolactone) (PCL, *w/v*) and 6% poly(lactic acid) (PLA, *w/v*) in a 7:3 (v/v) mixture of dichloromethane (DCM) and dimethylformamide (DMF). Additionally, 1 and 3% of CUR was incorporated into this mixture. The resulting solution was then loaded into an 8 mL special syringe. Subsequently, electrospinning was performed using the KH-1089 electrostatic spinning equipment with a 21G spinning needle. The operating voltage, distance, and rolling speed for electrospun were 18.5 kV, 15 cm, and 2000 rpm, respectively (Nano NC, Electrospinning System, Republic of Korea). The prepared electrospun fibers, designated PCP/CUR, are detailed in Table 1.

The CMCS was synthesized using a method adapted from Luo et al. (2018) [30]. Initially, 10 g of sodium hydroxide was weighed and dissolved in water to create a 50% aqueous solution. To this solution, 10.0 g of chitosan was added, and the mixture was thoroughly mixed, then frozen at −4 °C for 24 h. The alkali-treated chitosan was then transferred to a three-necked flask, and 200 mL of isopropanol was added. The mixture was mechanically stirred for 2 h until the chitosan was well dispersed. Following this, 15.0 g of monochloroacetic acid was added in two batches, and the reaction was allowed to proceed with continuous stirring at 60 °C for 5 h. After the reaction, the mixture was filtered and washed with absolute ethanol to obtain the crude product. The resulting product was dissolved in deionized water and dialyzed for 72 h. The final CMCS was freeze-dried using a freeze dryer (EYELA® Freeze Drying Unit 2200, Tokyo, Japan) and stored under constant temperature and dry conditions for future use. FTIR was used to characterize the lyophilized CMCS to study carboxymethylation.

To prepare the 3D printing ink, 10 mL of deionized water was heated on a magnetic stirrer set at 50 °C, and 8% gelatin (*w/v*) was dissolved completely. The solution was then stirred continuously while 2% CMCS (*w/v*) was added and dissolved thoroughly. PEDOT: PSS was subsequently incorporated at concentrations of 0, 0.25, 0.5, 1, and 2% (*v/v*) to create the final bioink. The mixtures were stirred until homogeneous. The prepared hydrogels were designated as GCP and are detailed in Table 2.

3D printing, & Preparation of biomimetic double-layer asymmetric PG hydrogel scaffold

SolidWorks software (Dassault Biosystems, USA) was used to build the target models, which were then exported as STL files. The open-source Slic3r v1.3.0 program was used to slice them, and the resulting G-code files were ultimately uploaded to the printer. A CELLINK BIO-X 3D bioprinter (Cellink Corporation, Sweden) with regulated nozzle and platform temperatures was used to print all of the hydrogels. With the nozzle temperature set to 37 °C, the platform temperature set to 10 °C, and the printing speed set to 2 mm/s, the produced GCP bioink was put into a syringe fitted with a 22G needle. The hydrogel scaffold height was 3 mm, and the model's dimensions were 20 × 20 mm. Table S1 lists the printing parameters. After printing, the hydrogel scaffolds were first crosslinked at 4 °C and then chemically crosslinked for 15 min at room temperature while submerged in a 0.25% glutaraldehyde (*w/v*) solution. The hydrogel scaffolds were then cleaned and freeze-dried for 2 days to characterize them.

To create a double-layer asymmetric scaffold by combining the external layer of PCP/CUR electrospun fibers and the internal layer of GCP hydrogel, the GCP hydrogel was directly printed onto the PCP/CUR electrospun fibers to form the PG hydrogel scaffold. In this study, PCL/PLA is referred to as PCP, Gelatin/CMCS/PEDOT: PSS as GCP, and the combination of PCP/CUR electrospun fibers and GCP hydrogel is designated as PG hydrogel scaffold. The hydrogel devoid of PEDOT: PSS was designated as the control group.

Chemical characterization

Morphological characterization

The surface structures of the PCP/CUR electrospun fibers and the GCP hydrogel were observed using Scanning Electron Microscopy (SEM) with an S-4800 instrument from Tokyo, Japan. Before testing, the samples were dried in a vacuum freeze dryer at −90 °C for 24 h to remove moisture, and each sample was sputtered with platinum (Pt). The elemental composition of the surface was analyzed using energy-dispersive X-ray Spectroscopy (EDS) mapping equipment connected to the SEM.

FTIR and XRD analysis

The Fourier-transform infrared (FTIR) spectra of PCP/CUR electrospun fibers and GCP hydrogel were recorded using a Perkin Elmer FTIR analyzer (Frontier, Perkin Elmer, UK) in the transmitted mode, covering a wavenumber range of 500–4000 cm^{-1} with a resolution of 4 cm^{-1}. The X-ray diffraction (XRD) patterns of PCP/CUR electrospun fibers and GCP hydrogel were acquired at room temperature using X'Pert PRO X-ray diffractometer (X'Pert PRO MPD, Philips, Eindhoven, Netherlands) with an operational voltage of 40 kV and a current of 40 Ma utilizing Cu Kα rays (λ = 1.5414 Å). The operational range (2θ) was 5–40°.

Contact angle measurement

The hydrophilicity of the PCP/CUR electrospun fibers was investigated through a contact angle analyzer (SEO-Phoenix MT (M.A.T), Malaysia). The hydrophilic properties of the samples were evaluated using the confined droplet approach. A 5 μL drop of water was dispensed by a syringe positioned vertically over the fiber surface. Following the application of water to the surface for 5–10 s, a charge-coupled device (CCD) camera quantified and documented the contact angle (θ) and the interfacial wetting energy. Each sample was tested in triplicate.

Mechanical characterization

The PCP/CUR electrospun fibers were prepared for mechanical property analysis. The tensile test was performed on a Universal Testing Machine (UTM; MCT-1150, AND Inc., Japan) at a constant speed of 10 mm/min. Compression testing of GCP hydrogels was performed on a Universal Testing Machine (UTM; MCT-1150, AND Inc., Japan) at a test speed of 10 mm/min. Young's modulus for each sample was calculated as the slope of the linear region of the stress-strain curve (strain range 3–5%), while toughness was measured as the area under the stress-strain curve.

Further, the rheological measurements of the GCP hydrogels were conducted using an ARES-G2 rheometer (TA Instruments, New Castle, Delaware, USA) with a 6 mm parallel plate setup. Strain-dependent measurements were conducted at 1 rad/s with strain ranging from 0.1% to 100%, while frequency-dependent tests were performed at 0.1% strain over 0.1–100 rad/s. Storage modulus (G′), loss modulus (G″), complex viscosity (η*), and shear stress (τ) were analyzed. All experiments were performed at room temperature.

Swelling rate and degradation

The swelling test was conducted to evaluate the hydrophilic-hydrophobic behavior of the fabricated PCP/CUR electrospun fibers and GCP hydrogels. For this, the dry weight of a certain amount of each sample was recorded (W_d). Next, the samples were immersed in PBS at 37 °C under static conditions. The samples were then blotted, and the swollen weight of each sample was recorded (W_s) at different time intervals (0, 0.5, 1, 2, 3, 6, 12, 24, 48 h) until equilibrium swelling was reached. The swelling ratio was calculated according to the following equation.

$$Swelling\,ratio\ (\%) = \left(\frac{W_s - W_d}{W_d}\right) \times\ 100\% \tag{1}$$

To further evaluate the degradation behavior of PCP/CUR electrospun fibers, samples were prepared and subjected to enzymatic degradation using trypsin enzyme and non-enzymatic degradation under different pH conditions. Electrospun fiber sheets were cut into uniform square Sect. (2 cm × 2 cm), and the initial dry weight (W_i) of each sample was recorded using an analytical balance. The samples were then immersed in 1 mL of phosphate buffer solutions at pH 4, pH 7.4, and pH 10, each containing 1 mg/mL of enzyme. The test tubes were incubated at 37 °C under shaking conditions to simulate physiological conditions and enhance enzymatic activity. At predetermined time points, the samples were carefully removed from the buffer solution, rinsed with deionized water to remove residual enzymes or buffer salts, and dried in a hot-air oven. The final dry weight (W_f) was measured, and the degradation percentage was calculated using the equation:

$$Degradation\,ratio\ (\%) = \left(\frac{W_i - W_f}{W_i}\right) \times\ 100\% \tag{2}$$

Additionally, the pH of the buffer solution was recorded at each time point to monitor potential changes during degradation. To assess the structural changes in the degraded electrospun fibers, scanning electron microscopy (SEM) was performed after gold sputter coating.

Drug release

To study the drug release behavior, PCP/CUR electrospun fibers of equal weight were immersed in a buffer solution (2% Tween 20 in PBS) at pH 7.4. The experiment was conducted with stirring at 150 rpm and 37 °C. At predetermined time intervals (0, 0.5, 1, 2, 3, 6, 12, 24, and 48 h), samples were collected for UV–vis analysis (OD at 425 nm) and immediately replaced with fresh buffer solution. The cumulative drug release was calculated using the following formula.

$$Drug\,release\;(\%) = \frac{D_{released}}{D_{total}} \times\; 100\% \tag{3}$$

where $D_{released}$ is the total amount of released CUR, and D_{total} is the amount of CUR incorporated in the electrospun fibers. The amount of released CUR was calculated based on a calibration curve of various concentrations. For accurate analysis, the experiment was repeated three times.

Electrochemical measurements

For electrochemical measurements of the developed hydrogels, cyclic voltammetry (CV) was conducted using a three-electrode setup with a working electrode, a reference electrode (Ag/AgCl), and a counter electrode (Pt). The glassy carbon electrode (GCE) was used as a working electrode to coat the hydrogel solution. For this, the GCE was polished with diamond-alumina paste and sonicated in a mixture of ethanol/acetone (1:1 ratio) for 15 min. After that, the GCE was washed with sterile DI water and dried before hydrogel coating. Next, 25–30 μL of hydrogel solution was drop-cast onto the surface of the GCE in the presence of Nafion (ionic conductivity $\sim 1.23 \times 10^{-2}$ Ω^{-1} cm^{-1}), and the resulting film was dried properly before CV measurement. After that, the GCP electrode was applied to a definite potential, and oxidation of the electrode began as soon as current began to flow. Electrochemical impedance was measured using electrochemical impedance spectroscopy (EIS) via a Nyquist plot. The conductivity (σ) of the hydrogel was calculated using Ohm's law (Eq. 4).

$$\sigma\; = \frac{L}{R * S} \tag{4}$$

Here, R represents the average resistance of the hydrogel, while L and S denote the length and cross-sectional area of the hydrogel, respectively. The average resistance was calculated from each voltage sweep, and three samples were tested for each hydrogel.

Design of the ES system

The configuration of the DC stimulation device is provided in the Supporting Information. A DC electric field (EF) stimulation device was fabricated to enable precise control of small-volume cell culture conditions (Figure S1(a)). The device comprised a stainless-steel lid and base (147 mm × 105 mm × 60 mm) specifically designed to accommodate a standard 6-well culture plate (Figure S1(b)). Each chamber contained a pair of rectangular platinum electrodes, which were connected to a regulated DC power supply. The electrical system was configured using a digital waveform generator (1-channel, 25 MHz, 250 MSa/s sampling rate; Tektronix Inc., Oregon, USA) coupled with a digital oscilloscope to ensure stable and accurate voltage output.

In vitro biocompatibility assay

HDF and HaCaT cells were cultured in DMEM containing 10% FBS and 1% P/S antibiotics at 37 °C in a humidified incubator with 5% CO_2 (Steri-Cycle 370 Incubator; Thermo-Fisher Scientific, USA). The cytotoxicity of the fabricated hydrogel scaffolds was evaluated using WST-8 and Live/Dead assays, with or without ES. Initially, ES (100 mV/25 min/day) was applied daily for up to 7 days to compare its effects. For the WST-8 assay, HDF and HaCaT cells were cultured individually (1×10^4 cells/100 μL medium) and/or co-cultured (1×10^4 cells each/100 μL medium) in 96-well plates. The experimental groups consisted of cells cultured on GCP hydrogel and on PCP/CUR electrospun fibers, while cells cultured without samples served as the control group. The cells were cultured for 1, 3, and 7 days. After incubation, 10% WST-8 reagent was added to each well, and the cells were incubated for an additional 2 h. The absorbance of the resulting formazan was measured at 450 nm, with 625 nm used as the reference wavelength.

For the Live/Dead assay, cultured cells (4×10^4 cells/2 mL/6-well) were treated with 10 μL of a 1:1 acridine orange/propidium iodide solution (1 mg/mL each) and incubated at 37 °C for 15 min. Images were immediately captured using a fluorescence microscope (DMi8 series, Leica Microsystems, Germany) with Leica Microsystems Suite X software (Leica Microsystems, Germany) under appropriate filter channels. The viability of the treated cells was quantified using Live/Dead fluorescence imaging after 1, 3, and 7 days of culture.

The number of Live/Dead cells was quantified using ImageJ software (v1.8, NIH, USA) equipped with the Live Cell Counter tool.

Cytoskeleton and cell migration study

The arrangement of F-actin and paxillin was investigated through fluorescence imaging to visualize the effect of the hydrogel scaffold on the cell cytoskeleton. The cytoskeletal morphology of HDF and HaCaT cells with and without ES was evaluated after 7 days of culture. For this, 2.5×10^4 cells were seeded on PG hydrogel scaffolds and cultured with respective samples. The cells were then exposed to 200 mV of ES for 25 min/day for 7 days. After the desired incubation period, the cells were washed with PBS, fixed with 3.7% PFA for 15 min, and then permeabilized with 0.1% Triton X-100 for 10 min. The permeabilized cells were washed twice with PBS and blocked with 1% BSA. The cells were then incubated with 200 µL of Alexa Fluor (AF) 555 F-actin probe (ex/em = 553/568) for 1 h to visualize F-actin. After actin staining, the cells were washed twice with PBS, and the nuclei were stained by adding 500 µL of DAPI solution for 2 min in the dark. After staining, the cells were rinsed, mounted with mounting media, and covered with a glass coverslip. Fluorescence images were captured using a fluorescence microscope (DMi8, Leica, Germany) at a magnification of 20x. The cell fluorescence intensity was measured using ImageJ software, and graphs were plotted using origin software. Corrected total cell fluorescence (CTCF) was calculated as follows:

$$\begin{array}{c} CTCF \\ = Integrated\ density \\ \left(\begin{array}{c} Area\ of\ selected\ cell \\ \times\ Mean\ fluorescence \\ of\ background\ readings \end{array} \right) \end{array} \qquad (5)$$

Because the HDF and HaCaT cells in PG hydrogel scaffolds were visually distinguishable under the microscope, their CTCF values were measured and compared with those of the control groups.

Cell migration assays were performed to evaluate the effects of PG hydrogel scaffolds and ES. To accomplish this, HDF and HaCaT cells were cultured in 6-well plates for 24 h to allow attachment, and then the cell monolayer was scraped using a 200 µL sterile pipette tip. After washing twice with 1x PBS to remove detached cells, the culture medium was replenished. ES (200 mV/25 min/day) was applied daily, and cells were observed under a microscope at 0, 24, and 48 h. Images of each well were captured at each time point. The scratch area percentage was measured using Image J, and the scratch closure percentage over 48 h was calculated using the following equation:

$$\begin{array}{c} Scratch\ closure\ (\%) \\ = \frac{\text{Scratch area at 0 h (\%)} - \text{Scratch area at 48 h (\%)}}{\text{Scratch area at 0 h (\%)}} \times 100\% \end{array} \qquad (6)$$

The degree of wound healing was determined based on the distance the cells migrated to the scratched area.

Analysis of reactive oxygen species (ROS)

The intracellular oxidative stress in HDF cells was evaluated using dichlorodihydrofluorescein diacetate (DCF-DA) fluorescence staining and 2, 2-diphenyl-2-picrylhydrazyl (DPPH) assay. Cells untreated with H_2O_2 were used as the negative control, whereas cells exposed to 200 µM H_2O_2 for 30 min were used as the positive control. After incubation at 37 °C, the cells were treated with 20 µM DCF-DA for 30 min and rinsed twice with PBS. Fluorescence intensity (Ex/Em = 485/538 nm) was measured using a fluorescence microscope, and intracellular ROS levels were quantified using ImageJ (NIH, USA).

Next, the antioxidant efficiency of the samples was evaluated by measuring their ability to scavenge the stable free radical DPPH [31]. Typically, 1.0 mg of the prepared PG hydrogel scaffold was added to 500 µL of 100 µM (100×10^{-6} M) DPPH solution in ethanol. The mixture was then incubated in the dark for 30 min. Subsequently, the absorbance was measured at 517 nm using a UV–vis spectrophotometer (Infinite® M Nano 200 Pro; TECAN, Switzerland). The radical scavenging capacity of the hydrogel was calculated using a standard equation.

All results were obtained from three independent experiments and are presented as mean ± SD ($n = 3$).

$$Radical\ scavenging\ effect\ (\%) = \frac{A_B - A_S}{A_B} \times 100\% \qquad (7)$$

where A_B and A_S are the absorbance values of the blank (DPPH + ethanol) and the samples (DPPH + ethanol + sample), respectively.

RNA isolation and real-time PCR (qRT-PCR) analysis

The expression of marker genes in PG hydrogel scaffolds-treated cells was evaluated using qRT-PCR based on the presence or absence of ES stimulation. Briefly, cells (4×10^4 cells/100 µL medium) were cultured in DMEM in 6-well plates for 7 days, and the cells were exposed to ES (200 mV for 25 min/day). RNA was extracted using TRIzol® reagent following the manufacturer's instructions. The purity and concentration of the extracted RNA were assessed using a spectrophotometer. cDNA was synthesized, and PCR was performed from 2 µg of RNA using reverse transcriptase and SYBR Green Master mix. mRNA expression was quantified using Bio-Rad Real-Time PCR (CFX96TM Maestro Real-Time System, Bio-Rad, USA). The reaction conditions included 43 cycles of denaturation at 95 °C for 15 s and amplification at 60 °C for 1 min. All experiments were performed in triplicate, and data were normalized to the housekeeping gene GAPDH. Relative mRNA expression of HDF and HaCaT was compared using histograms. Details of the primers used in this study are listed in Table S2.

Immunocytochemical staining of marker protein

The expression of marker proteins was assessed by immunocytochemistry. HDF cells (4×10^4 cells/100 µL medium) were cultured in 6-well plates with PG hydrogel scaffolds and treated for 7 days. Cell staining was performed after washing with PBS, followed by fixation with 3.7% PFA at room temperature for 15 min. Permeabilization was performed by incubating the cells with 0.1% Triton X-100 at room temperature for 10 min. The cells were then washed twice with PBS, blocked with 1% BSA, and incubated with 250 µL of mouse monoclonal antibodies targeting fibronectin. The nuclei were counterstained with 20 µL of 1 mg/mL DAPI solution for 2 min in the dark. Following staining, the cells were washed, mounted with mounting media, and a glass coverslip was placed on top. Fluorescent images were captured at 20x magnification using a fluorescence microscope.

Antibacterial and anti-biofilm efficiency

The antibacterial properties of the PG hydrogel scaffolds were evaluated against *Escherichia coli* (*E. coli*) and methicillin-resistant *Staphylococcus aureus* (MRSA). For antibacterial tests, fresh bacterial cultures were prepared by inoculating a single colony from stock cultures into Nutrient Broth (NB) and incubating overnight at 37 °C with shaking at 100 rpm. The optical density (OD_{600}) of the bacterial cultures was adjusted to 0.09 ± 0.01. Sterilized PG hydrogel scaffolds of equal weight were used for testing, and wells without hydrogel scaffolds served as controls. The bacterial cultures were incubated under two conditions: without electrical stimulation (-ES) and with electrical stimulation (+ ES). Incubation was carried out for 6 and 12 h. After exposure, bacterial viability was assessed using colony-forming unit (CFU) analysis. The cultures were serially diluted up to 10^{-4} in phosphate-buffered saline (PBS), and 100 µL of each dilution was plated on NB agar plates. These plates were incubated at 37 °C for 24 h, and the average CFU per milliliter was calculated. Relative bacterial viability was assessed by comparing the CFU counts of the samples with those of the control group, in which bacteria were grown without hydrogel scaffolds or stimulation.

The antibacterial efficiency was calculated using the following equation.

$$Antibacterial\ efficiency\left(\frac{CFU}{plate}\right)(\%) = \frac{CFU_{control} - CFU_{treatment}}{CFU_{control}} \times 100\% \quad (8)$$

where $CFU_{control}$ represents the total CFU in the control group and $CFU_{treatment}$ represents the total CFU in the experimental group.

The anti-biofilm properties of the PG hydrogel scaffolds were evaluated independently of their antibacterial effects to distinguish their efficiency in inhibiting biofilm formation. For the antibiofilm analysis, the bacterial culture was diluted to an OD600 of 0.09 ± 0.01 and inoculated into 6-well plates, then incubated at 37 °C for 48 h to form biofilms. PG hydrogel scaffold extracts were added to the culture medium, while a bacterial culture with pure media was used as the control. The samples were incubated with the biofilm for 12 h to evaluate their effect on biofilm formation and inhibition. After incubation, the supernatant was carefully removed, leaving the biofilm in the wells. Then, 0.1% crystal violet stain was added for 20 min, and the stain was removed by washing with PBS and drying. The retained stain was dissolved in 95% ethanol, and the absorbance was measured at 490 nm using a UV spectrophotometer (Table 3).

Statistical analysis

Statistical analysis was performed using OriginPro 9.0 software. Statistical significance between the control

Table 3 Comparison of antibacterial efficacy with ES: A review of previous and recent studies

Formulations	Stimuli	Time	Type of bacteria	Advantage	Limitations	Ref.
Mg-Al LDH, PTFE, Minocycline	± 8 V, 3 Hz	48 h	*S. aureus*, *E. coli*	The strong antibacterial effect, even at low voltage, 100% drug release rate achieved	Relatively lower antibacterial effect on *E. coli*	[96]
PPY/Chitosan Film @ Gentamicin	DC (200 µA)	48 h	*S. aureus*	50x reduction in biofilm bacteria	DC + gentamicin, Biofilm reduction, Bacterial autolysis, Increased sensitivity	[97]
CNT, Polyvinylidene fluoride	DC (< 3 V)	21 h	*P. aeruginosa*	Biofilm dissolution, recovery of membrane permeability	Effective only within the limited treatment time, reliant on H_2O_2 electrochemical generation	[98]
PEDOT, Zn	0.75 V	30 min	*E. coli*, *S. aureus*	High antibacterial efficacy, strong biofilm disruption, enhances chronic wound healing	Dependent on battery configuration and current	[99]
PG hydrogel scaffold (GCP hydrogel @ PCP/CUR electrospun fiber)	DC (200 mV/mm, 25 Hz)	25 min	*E. coli*, MRSA	High antibacterial efficacy, enhanced cell proliferation and migration, Strong biofilm disruption; Accelerates chronic wound healing	Requires optimization for clinical application; Potential long-term effects of ES	This study

and treatment groups was determined using one-way ANOVA. All the data are presented as mean ± SDs. Differences were considered significant at * $p < 0.05$, ** $p < 0.01$, and *** $p < 0.001$.

Results and discussion

Synthesis and morphological characterization of PG hydrogel scaffolds

Electrospinning of PCP/CUR electrospun fibers and 3D printing of GCP hydrogel

A blend solution was prepared by dissolving 12% poly(ε-caprolactone) (PCL, w/v) and 6% poly(lactic acid) (PLA, w/v) in a mixture of dichlorom00ethane (DCM) and dimethylformamide (DMF) in a 7:3 (v/v) ratio. Additionally, 1% and 3% CUR were incorporated into this mixture. The PCP/CUR electrospun fiber layer was then prepared through electrospinning. The resulting electrospun fibers were designated as PC, PCP, PCP/CUR-1, and PCP/CUR-3 based on their composition. Figure 2(a) represents the SEM images of electrospun fibers. The outer layer of the PCP/CUR electrospun fiber membrane, depending on CUR content, shows a tightly connected mesh structure with a uniform bead-free morphology across all samples. Pure PCL electrospun fibers displayed a smooth structure with an average diameter of 33.66 ± 2 μm, while the addition of PLA reduced the diameter to 13.57 ± 0.1 μm (Figure S2(a)). Additionally, as the CUR concentration increased, the average diameter of PCL/PLA electrospun fibers decreased, indicating that CUR content influences electrospun fiber diameter. According to previous studies, the addition of polar CUR increases the conductivity of the electrospinning solution, enhancing the electrical drawing effect and thus facilitating fiber miniaturization [32, 33]. Consequently, electrospun fibers containing 1 and 3 wt% CUR exhibited average diameters of 11.24 ± 2 μm and 5.30 ± 0.2 μm, respectively.

Next, GCP hydrogel ink was prepared by thoroughly mixing and homogenizing a Gelatin/CMCS solution with PEDOT: PSS. To achieve high conductivity and excellent processability simultaneously in conductive polymer hydrogels, the hydrogel must be designed with a conductive network and tunable rheological properties [34, 35]. For this purpose, PEDOT: PSS was selected as the conductive network, and Gelatin/CMCS was chosen as the mechanical matrix to enhance the rheological properties suitable for 3D printing. The ink was prepared with five different molar concentrations of PEDOT: PSS, designated GCP_0, $GCP_{0.2}5$, $GCP_{0.5}$, GCP1, and GCP_2, respectively. As the PEDOT: PSS concentration increased, the hydrogel exhibited a deep blue color, indicating that PEDOT: PSS was uniformly distributed within the hydrogel. In contrast, the hydrogel without PEDOT: PSS appeared almost transparent (Figure S2(b)).

The viscosity of the ink increased with higher PEDOT: PSS concentrations, significantly affecting 3D printing performance. At PEDOT: PSS concentrations below 0.5%, the ink exhibited severe lateral spreading on the substrate, while concentrations exceeding 2% led to extrusion discontinuity and nozzle clogging. However, PEDOT: PSS concentrations between 0.5% and 2% demonstrated rheological properties suitable for 3D printing. The fabricated GCP hydrogel ink exhibited excellent printability, enabling the precise printing of complex hydrogel scaffold structures measuring 20 mm × 20 mm × 3 mm. The CAD model of the fabricated hydrogel is illustrated in Fig. 2(b). The hydrogel scaffold model was designed in SolidWorks (Dassault Systems, USA) and exported as an STL file for compatibility with the CELLINK BIO-X printer (Cellink Corporation, Sweden). The printed structures maintained high shape fidelity and stability without lateral spreading or collapse. Figure 2**(c)** shows SEM images of 3D printed GCP hydrogels, displaying a three-dimensional porous network structure with evenly distributed PEDOT: PSS. As the concentration of PEDOT: PSS increases, the pore diameter of the GCP hydrogel decreases from 201.94 μm to 64.94 μm (Figure S2(c)). The incorporation of PEDOT: PSS reduces pore size and promotes a uniform pore distribution, thereby improving mechanical properties. This is due to the viscosity of the PEDOT: PSS dispersion, which reduces pore size. PEDOT: PSS may act as a physical crosslinking point within the GCP hydrogel. This three-dimensional porous structure provides an ideal environment that promotes cell adhesion, migration, and proliferation, resembling the natural ECM [36]. In addition, the 0°/90° cross-hatch pattern used during 3D printing exhibits structural characteristics that can mimic the anisotropy of the ECM, providing a physical foundation favorable for directional cell proliferation and tissue organization [37].

Structure of the PG hydrogel scaffolds mimicking the native skin model

The PG hydrogel scaffolds are designed as a double-layer asymmetric structure for skin wound healing (Fig. 2(d)), consisting of a hydrogel layer that promotes healing and an electrospun fiber layer containing CUR that prevents bacterial invasion. For this, the electrospun PCP/CUR layer was placed on a Petri plate, and a GCP hydrogel was printed on it using an extrusion printer. These components work together to enhance the wound healing process and provide a protective barrier against pathogens, mimicking the natural skin function [38].

The biologically active GCP hydrogel was printed onto the electrospun PCP/CUR layer, followed by crosslinking with 0.25% glutaraldehyde. The PCP/CUR electrospun fibers exhibit a yellow color indicative of the presence of CUR, while the 3D-printed GCP forms a fine,

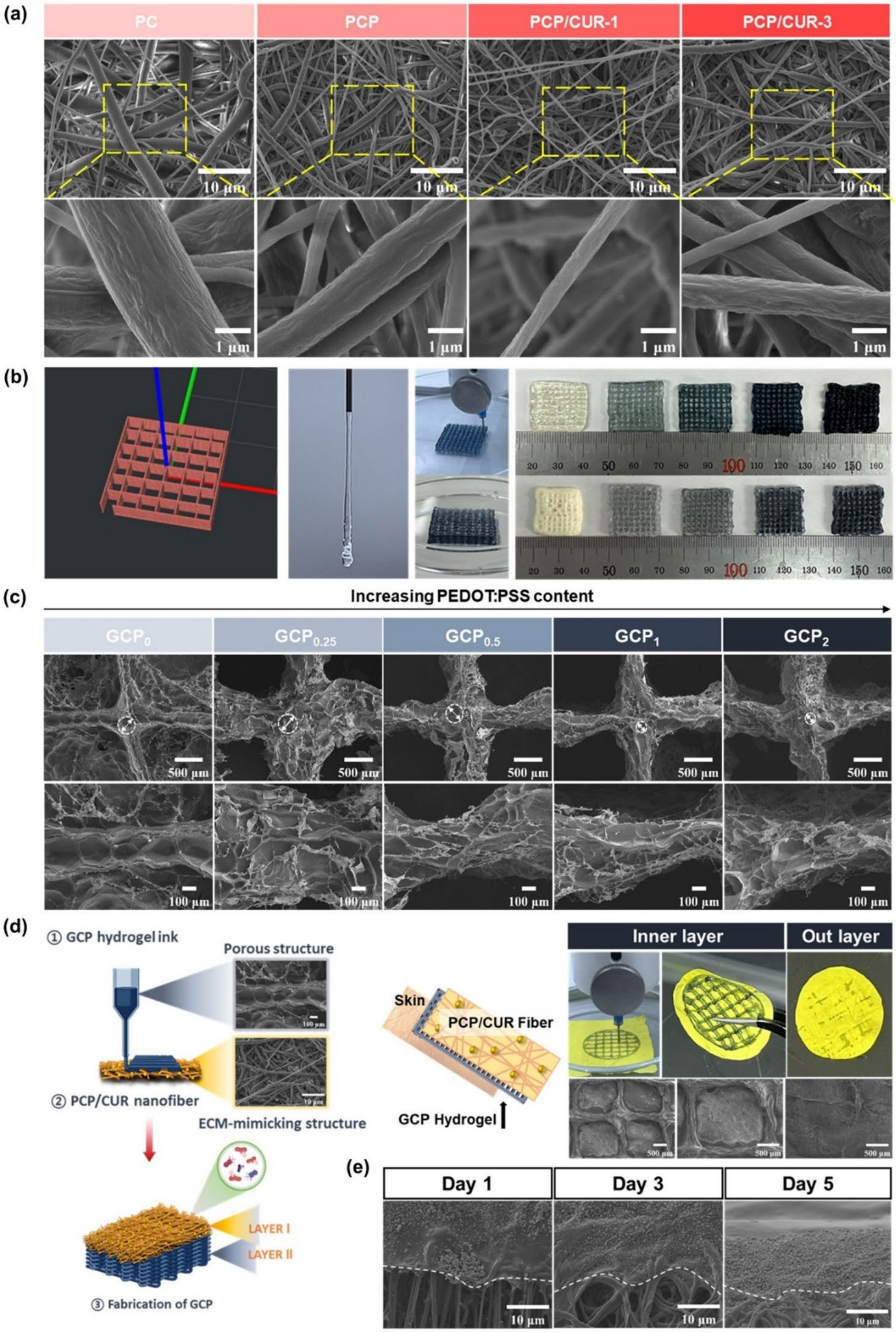

Fig. 2 **(a)** SEM image showing the detailed structure of PCP/CUR electrospun fibers. Scale bar: 10 µm. **(b)** 3D model design and photograph of the 3D-printed GCP hydrogel scaffold. **(c)** The SEM image shows the detailed structure of the printed GCP hydrogel, highlighting its porous network. Scale bar: 500 µm. **(d)** Schematic and SEM images of the PG hydrogel scaffold showing its double-layer structure and strong interlayer bonding. Scale bar: 500 µm. **(e)** SEM images of composite hydrogel scaffold cross-sections after incubation in NaCl saline (pH = 7) for 1, 3, and 5 days. Scale bar: 10 µm

uniform three-dimensional multilayer structure with a blue hue due to the presence of PEDOT: PSS. There was no change when the hydrogel was printed onto the electrospun fibers, and the SEM images reveal the delicate structure of the electrospun fibers and the uniform distribution of the hydrogel, confirming a strong bond between the two layers.

The PG hydrogel scaffolds were incubated in NaCl solution, mimicking physiological ionic conditions, for 1, 3, and 5 days to evaluate the adhesion and structural

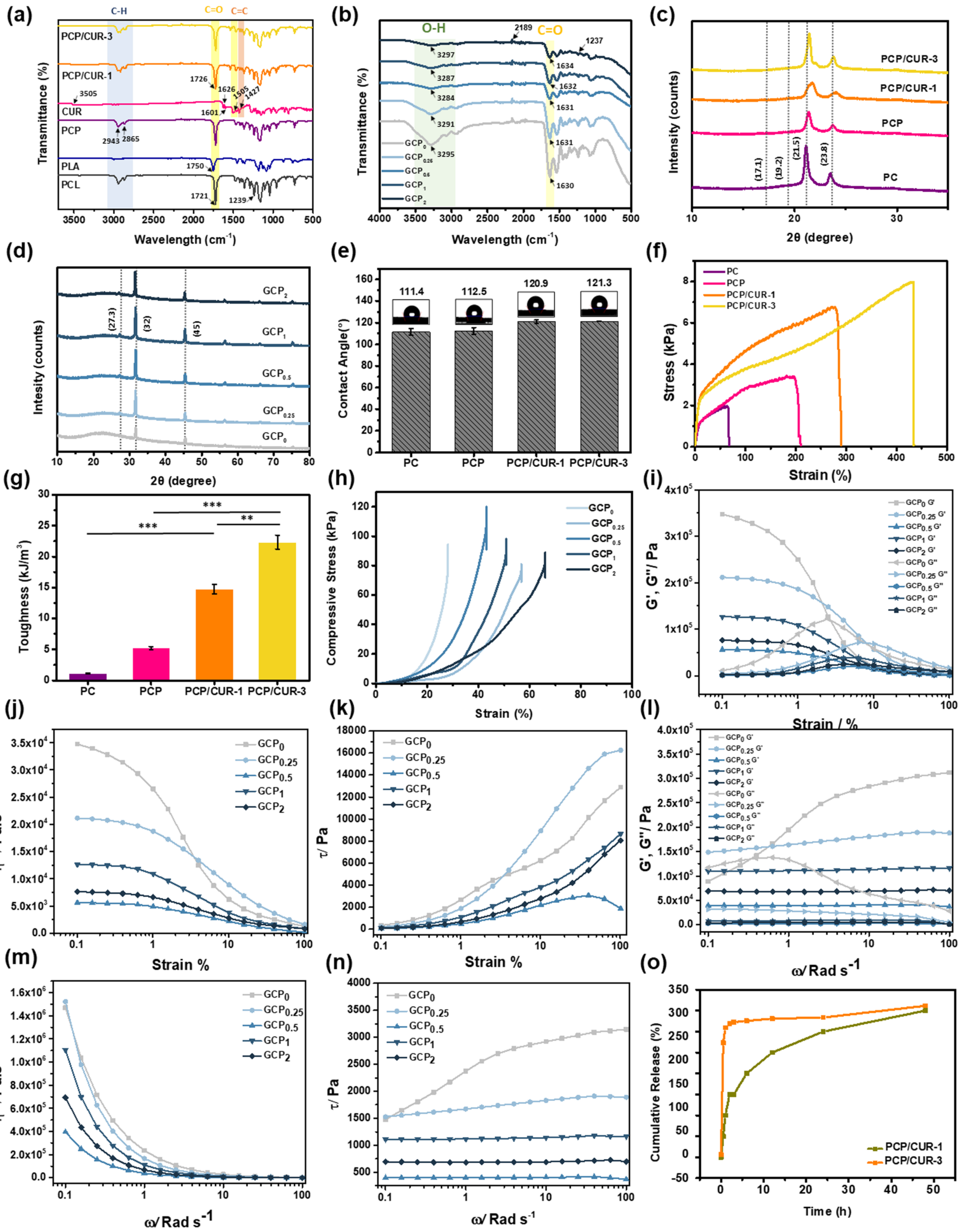

Fig. 3 (See legend on next page.)

(See figure on previous page.)

Fig. 3 Characterization of PG hydrogel scaffolds **(a)** FTIR spectra showing the functional groups of PCL, PLA, and PCP/CUR electrospun fibers. **(b)** FTIR spectra of the GCP conductive hydrogels. **(c)** XRD patterns of PCP/CUR electrospun fibers, showing the crystallinity of PCL, PLA, and CUR. **(d)** XRD patterns of the GCP hydrogels. **(e)** WCA of PCL, PCP, and PCP/CUR electrospun fibers with varying CUR content. **(f)** Tensile strength and **(g)** toughness at the break for PC, PCP, PCP/CUR-1, and PCP/CUR-3 electrospun fibers. **(h)** Compressive stress and strain of GCP hydrogels. Strain-dependent GCP Hydrogel: **(i)** Change in storage modulus (G′) and loss modulus (G″). **(j)** Change in complex viscosity (η*) and shear stress (τ). **(k)** Change in shear stress (τ). Frequency-dependent GCP Hydrogel: **(l)** Change in storage modulus (G′) and loss modulus (G″). **(m)** Change in complex viscosity (η*). **(n)** Change in shear stress (τ). **(o)** Cumulative release profile of PCP/CUR nanofibers in PBS (pH 7.4) over 48 h

stability between the hydrogel and electrospun fiber layers. SEM images demonstrated that the cross-sectional structure of the scaffolds remained well-defined throughout the incubation period (Fig. 2(e)), indicating that the strong bonding between the two layers effectively maintains structural integrity. For this experiment, the PG hydrogel scaffold, combining the conductive hydrogel and electrospun fiber layer, was used, confirming its structural stability and suitability for application at the wound site.

Energy-dispersive spectroscopy (EDS) mapping images of freeze-dried GCP hydrogels confirm that the C, N, and O elements are uniformly distributed (Figure S2(d)). The C and O elements originate from gelatin [39], the C, N, and O elements from CMCS [40], and the S element from PEDOT: PSS [41], indicating that PEDOT: PSS is evenly distributed within the GCP hydrogel [42].

Interaction and crystallinity of PG hydrogel scaffold

FTIR spectrum analysis revealed the key functional groups of electrospun fibers (Fig. 3(a)). PCL showed characteristic peaks for ester group C = O absorption at 1721 cm^{-1} and C–O–C asymmetric stretching at 1239 cm^{-1} [43], while PLA exhibited a C = O stretching peak at 1750 cm^{-1} [44]. These peaks were also observed in the electrospun fibers of PCL and PLA blend (PCP), indicating that the chemical structure of both components is preserved and they are physically combined. Additionally, the electrospun fibers of PCP showed characteristic peaks for C–H stretching at 2943 cm^{-1} and 2865 cm^{-1}, as well as C = O carbonyl stretching at 1721 cm^{-1}. This confirms that the inherent properties of PCL, such as hydrophobicity, and PLA, such as mechanical strength, are maintained after electrospinning. CUR exhibited characteristic peaks at 3505 cm^{-1} for O–H stretching, 1626 cm^{-1} for C = C, 1601 cm^{-1} for C = O, 1427 cm^{-1} for aromatic C = C stretching, and 1505 cm^{-1} for mixed C = O stretching and in-plane bending vibrations, reflecting the intrinsic chemical properties of CUR [45]. In the FTIR spectrum of CUR-loaded PCL/PLA blended electrospun fibers (PCP/CUR-1,3), these characteristic peaks of CUR were observed at 1505 cm^{-1} and 1427 cm^{-1}, and a sharp peak was detected at 1726 cm^{-1}, suggesting interactions with PLA and PCL chains. Furthermore, a change in the shape and increased intensity of the –OH peak in the electrospun matrix containing CUR indicated a weak hydrogen bonding interaction between CUR and PCP.

According to previous studies, the hydrophobic properties of PCP/CUR containing CUR contribute to the structural stability of electrospun fibers, potentially promoting sustained release of CUR over an extended period [46].

The FTIR spectra for CS and CMCS are shown in Figure S3(a). For CS, the broad absorption peak at 3288 cm^{-1} corresponds to overlapping N-H and O-H stretching vibrations. In comparison, peaks at 1650 cm^{-1}, 1613 cm^{-1}, and 1059 cm^{-1} are attributed to the amide I band, the N-H bending vibration, and the C6-OH, respectively [47]. In the FTIR spectrum of CMCS, the disappearance of the 1650 cm^{-1} peak indicates the breakdown of the amide bond. Instead, two prominent peaks at 1590 cm^{-1} and 1423 cm^{-1} emerge, representing the asymmetric and symmetric stretching vibrations of COO^{-}. These findings confirm the successful introduction of COO^{-} groups into the chitosan chain [48]. Additionally, the reduction or absence of the 1059 cm^{-1} peak suggests that the substitution reaction occurred primarily at the C$_6$-OH site. This confirms the successful carboxymethylation of chitosan to form CMCS.

Furthermore, the FTIR spectra of the GCP conductive hydrogel are presented in Figure S3(b). In the FTIR spectrum of gelatin, a peak at approximately 1640 cm^{-1}, corresponding to the C = O stretching vibration (amide I band), was observed [49]. This indicates that the amide bonds in Gelatin are preserved within the hydrogel. For CMCS, a broad peak in the range of 3200–3500 cm^{-1} was observed, corresponding to the -OH group [50]. In the case of PEDOT: PSS, a peak at 1237 cm^{-1} corresponding to the S = O stretching vibration was observed, indicating the characteristics of PSS in PEDOT [51].

Additionally, peaks at 2189 cm^{-1} and 1630 cm^{-1}, associated with C ≡ C bond stretching and C = C bond deformation vibrations, respectively, support the conductive properties of PEDOT: PSS. Furthermore, as doped PEDOT: PSS was mixed into the hydrogel solution, the peak intensity in the FTIR spectrum became more flattened (Fig. 3(b)) [52]. This is interpreted as the breaking of thiophene ring bonds in PEDOT: PSS, which then formed bonds with the amide groups in chitosan and gelatin [53]. In the hydrogel containing glutaraldehyde, the peaks were enhanced compared to those in other samples, indicating that glutaraldehyde reacted with the amide groups of chitosan and gelatin, forming new conjugated structures via the Schiff base reaction.

These results demonstrate that the GCP conductive hydrogel retains the chemical characteristics of each component, with the biocompatibility of Gelatin, the moisture retention ability of CMCS, and the conductivity of PEDOT: PSS, showing the potential of this hydrogel as a multifunctional conductive material.

Conformational alterations in the hydrogel scaffold were analyzed using XRD investigation. The XRD of PCP/CUR electrospun fibers is shown in Fig. 3(c). In CUR-loaded PCP/CUR electrospun fibers, two characteristic diffraction peaks corresponding to the PLA phase (2θ ~ 17.1° and ~ 19.2°) [54, 55] and two characteristic diffraction peaks corresponding to the PCL phase (2θ ~ 21.5° and ~ 23.8°) were observed. The lower intensity of the diffraction peaks for the PLA phase is attributed to its lower crystallinity compared to the PCL phase. Additionally, as the CUR content increased from 1% to 3%, the diffraction peaks for PCP/CUR-1 and PCP/CUR-3 decreased. Previous studies have indicated that the crystalline regions of the PLA and PCL phases tend to encapsulate CUR, thereby reducing its crystallinity [56].

Additionally, the XRD analysis of the GCP conductive hydrogel was compared with the GCP_0 (control) sample, as shown in Fig. 3(d). According to Kim et al. (2014)., the XRD pattern shows characteristic peaks at 2θ = 3.8°, 6.6°, 17.7°, and 25.6° [57], which represent the amorphous halo diffraction of PSS and the interchain packing of PEDOT: PSS [58]. In this study, the presence of PEDOT: PSS in the GCP hydrogel was identified at 27.3° in GCP_0 and 27.1° in GCP_2. As the concentration of PEDOT: PSS increased, the peak intensity showed a decreasing trend, suggesting that the integration and interaction between gelatin, chitosan, and PEDOT: PSS led to a reduction in the crystallinity of the composite hydrogel scaffold. These results indicate that the GCP conductive hydrogel possesses an amorphous structure and that PEDOT: PSS is effectively dispersed within the hydrogel.

The incorporation of CUR increases the hydrophobicity of the electrospun fibers

The wettability of electrospun fibers plays a crucial role in drug release from the matrix into an aqueous environment [59, 60]. In addition to the polymer's characteristics, the surface roughness of electrospun fibers significantly impacts wettability [61]. Analysis of hydrophobic changes in electrospun fibers with varying CUR content, measured by contact angle, revealed that all fibers showed hydrophobicity with contact angles exceeding 100° (Fig. 3(e)). PCL alone recorded a contact angle of 111.4°, while electrospun fibers of blended PCL and PLA (PCP) showed a slight increase to 112.5°. With increased CUR content, PCP/CUR-1 had a contact angle of 120.9°, and PCP/CUR-3 showed the highest contact angle of 121.3°. These findings indicate that as CUR content increases, the hydrophobicity of electrospun fibers gradually rises, suggesting that CUR-infused electrospun fibers tend to reduce interaction with water and enhance hydrophobicity.

Mechanical properties of PG hydrogel scaffolds

Electrospun fibers must possess sufficient mechanical strength to be used as wound dressings [62]. In this study, tensile tests were conducted to compare the mechanical properties of PC, PCP, PCP/CUR-1, and PCP/CUR-3 electrospun fibers (Fig. 3(f, g). PC electrospun fibers exhibited a tensile strength of 1.9 kPa, a toughness of 1.15 kJ/m^3, and an elongation at break of 66%. In contrast, PCP electrospun fibers showed a tensile strength of 3.4 kPa, a toughness of 5.24 kJ/m^3, and an elongation at break of 193.7%, indicating that adjusting the ratio of PCL and PLA in the PCP composite improved the mechanical properties compared to using PCL alone [63]. Furthermore, PCP/CUR-3 electrospun fibers with CUR loading exhibited a tensile strength of 8 kPa, a toughness of 22.35 kJ/m^3, and an elongation at break of 433.54%, showing a significant increase in both tensile strength and elongation due to the inclusion of CUR. This demonstrates the excellent compatibility between CUR and PCP. Therefore, in this study, PCP/CUR electrospun fibers with an optimal fiber diameter and superior mechanical strength were selected as the outer layer of the PG hydrogel scaffolds.

Mechanical properties are critical indicators for flexible deformation sensors [64, 65]. To investigate the mechanical properties of GCP hydrogels and analyze the effect of PEDOT: PSS content on the hydrogel structure, compressive stress tests were performed. The results revealed contrasting effects of PEDOT: PSS concentration on compressive stress and strain (Fig. 3(h)). Under compressive stress, the GCP hydrogel without PEDOT: PSS exhibited a maximum compressive stress of 94.4 kPa. With an increase in PEDOT: PSS concentration to 0.5 wt%, the $GCP_{0.5}$ hydrogel showed an enhanced compressive stress of~ 120 kPa. However, further increasing the PEDOT: PSS concentration to 2 wt% (GCP_2) resulted in a reduced compressive stress of 89 kPa. This reduction is attributed to the formation of a porous structure within the hydrogel due to PEDOT: PSS, which lowers the network density and weakens the compressive strength.

In contrast, the strain showed a significant increase with higher PEDOT: PSS concentrations. The GCP hydrogel without PEDOT: PSS demonstrated a maximum strain of 28.1%, while the $GCP_{0.5}$ and GCP_2 hydrogels exhibited 43.2% and 67.2% maximum strain, respectively. This increase is likely due to the enhanced porosity introduced by PEDOT: PSS, which makes the network more flexible and allows greater deformation under external loads.

The observed decrease in compressive stress and increase in strain with higher PEDOT: PSS concentrations suggest that these hydrogels are particularly suitable for applications requiring both flexibility and electrical conductivity, such as bioelectronic devices [66].

To further evaluate the mechanical properties of the GCP hydrogels, we analyzed the storage modulus (G′), loss modulus (G″), complex viscosity (η*), and shear stress (τ) as functions of strain and angular frequency (Fig. 3(i)). For the GCP_0, the storage modulus (G′) measured approximately 3.5×10^5 Pa at a low strain of 0.1%, and it gradually decreased to about 0.2×10^5 Pa at a 10% strain, indicating a weakening of the network with increasing strain. The loss modulus (G″) was measured to be approximately 0.6×10^5 Pa. In contrast, the PEDOT: PSS incorporated hydrogel, GCP_2, started with a G′ of approximately 0.76×10^5 Pa at 0.1% strain, which decreased more rapidly to around 0.18×10^5 Pa with increasing strain, while the G″ remained near 0.21×10^5 Pa. This suggests an increased contribution of viscous (loss) properties upon the incorporation of PEDOT: PSS. In both samples, the complex viscosity (η*) decreased with increasing strain, indicative of shear-thinning behavior (Fig. 3(j)). Specifically, GCP_0 decreased from about 3.4×10^4 Pa·s at 0.1% strain to roughly 1.3×10^3 Pa·s at 100% strain, whereas GCP_2 decreased from about 7.6×10^3 Pa·s to approximately 0.8×10^3 Pa·s under the same conditions. The shear stress (τ) at 100% strain was approximately 12.896×10^3 Pa for GCP_0, while it was about 8.071×10^3 Pa for GCP_2, further confirming that an increase in PEDOT: PSS content reduces the overall network strength and shear stress (Fig. 3(k)). When examining the frequency dependence (Fig. 3(l)), for $GCP_{0,}$ the storage modulus (G′) was about 8.9×10^4 Pa at 0.1 rad/s and slightly increased to approximately 3.1×10^5 Pa at 100 rad/s, with the loss modulus (G″) maintaining a level around 1.4×10^5 Pa. In the case of GCP_2, G′ increased from about 6.9×10^4 Pa at 0.1 rad/s to roughly 7.0×10^4 Pa at 100 rad/s, consistently remaining lower than that of GCP_0, which indicates an overall reduced network strength. Similarly, the complex viscosity (η*) for GCP_0 decreased from about 1.5×10^6 Pa·s at 0.1 rad/s to approximately 3.1×10^3 Pa·s at 100 rad/s, and for $GCP_{2,}$ it dropped from around 6.9×10^5 Pa·s to about 0.7×10^3 Pa·s, further demonstrating the pronounced shear thinning behavior with increasing frequency (Fig. 3(m)). The shear stress at 100 rad/s was found to be about 3.146×10^3 Pa for GCP_0 and around 0.7×10^3 Pa for GCP_2, confirming that higher PEDOT: PSS content leads to lower stress levels (Fig. 3(n)).

In summary, increasing the PEDOT: PSS content results in a significant decrease in the storage modulus (G′) and shear stress (τ), indicating a weakened hydrogel network. At the same time, the loss modulus (G″) becomes relatively more prominent, suggesting a shift toward more viscous behavior. Moreover, the marked decrease in complex viscosity with increasing strain and frequency, indicative of shear-thinning behavior, indicates that the PEDOT: PSS-incorporated hydrogel is more flexible and flowable, yet it possesses lower mechanical strength and network rigidity than the GCP_0. From these results, we can conclude that the inclusion of PEDOT: PSS led to a more flexible and adaptive hydrogel network, as evidenced by the decrease in storage modulus (G′) and shear stress (τ). The transition to enhanced viscous behavior, indicated by the elevated loss modulus (G″), implies greater compliance, rendering the hydrogel more adaptable to dynamic wound conditions. The significant shear-thinning effect enhances injectability and application convenience, enabling improved conformity to uneven wound surfaces while preserving conductivity for superior wound healing.

Swelling ratio & degradation of PCP/CUR

The healing process is closely related to wound exudate formation, and excessive exudate can hinder cell migration to the wound surface, potentially extending the wound healing period [67]. The swelling behavior of CUR-loaded PCP/CUR electrospun fibers was recorded over 48 h, and the results are shown in Figure S3(c). A significant increase in swelling was observed during the first 10 h for the PCP/CUR electrospun fibers. Additionally, the swelling increased with increasing CUR content, with the maximum value observed in PCP/CUR-3. This suggests that the diffusion of the CUR release into the inner layers of the mixed PCP/CUR electrospun fibers was greater, which may have a positive impact on drug release [68, 69].

The water-absorption capacity of hydrogels affects various properties, such as pore size, mechanical characteristics, and the electrical properties of conductive hydrogels, which ultimately influence cellular behavior [70, 71]. The swelling ratio of GCP hydrogels was monitored over time by incubating previously freeze-dried samples in PBS (pH 7.4, 37 °C). The pure Gelatin/CMCS hydrogel exhibited rapid swelling, reaching a maximum swelling ratio of approximately 1500%. In contrast, the composite gels containing PEDOT: PSS showed a significantly reduced swelling ratio of around 500–800% (Figure S3(d)), with the water absorption capacity decreasing as the concentration of PEDOT: PSS increased. All hydrogels reached their maximum swelling ratio after being incubated in PBS at 37 °C for 24 h. These findings support previous studies indicating that PEDOT: PSS content affects the water-absorption capacity of hydrogels.

During the wound healing process, the pH of the body continuously changes, and enzymes are released to aid healing [72]. To assess the biodegradability of electrospun fibers in a similar environment, experiments were conducted at pH 4, 7.4, and 10, with and without enzymes. SEM images confirmed that the presence of CUR delayed the degradation of the electrospun fibers [73, 74] (Figure S4(a, f)). Similarly, additional results demonstrate that fiber degradation proceeded more rapidly in the presence of enzymes (Figure S4 (b-e, g-j)). The lowest degree of electrospun fiber biodegradation was observed at pH 4. Given PCL's slow degradation rate, it is advantageous for long-term wound healing scenarios, such as in diabetic wounds. As the CUR concentration in the PCL/PLA solution increased from 1% to 3%, the biodegradability of the resulting electrospun fibers decreased.

The incorporation of PEDOT: PSS imparts conductivity to the hydrogel

As described in Sect. 2.3.1, CMCS was synthesized from chitosan (Figure S5(a)). The addition of PEDOT: PSS to the conductive hydrogel increased its electrical conductivity compared with the pure Gelatin/CMCS hydrogel. With the increase in PEDOT: PSS content from 0 to 2 wt%, the electrical conductivity of the hydrogel gradually increased from GCP_0 ($\approx 0.06 \pm 0.03$ S m^{-1}) to GCP_2 ($\approx 0.16 \pm 0.14$ S m^{-1}), as shown in Figure S5(b). Notably, native skin exhibits electrical conductivity in the range of approximately 1×10^{-5}–0.26 S m^{-1}, and materials within this range are known to facilitate intercellular signaling, thereby promoting wound healing. The conductivity of the GCP hydrogel falls within this physiologically relevant range, suggesting its potential to enhance cellular communication and tissue regeneration at wound sites. This enhancement in electrical conductivity can be attributed to the formation of a conductive PEDOT: PSS network and to changes in the porous structure of the hydrogel [75]. With higher concentrations of PEDOT: PSS, more pores were formed within the hydrogel, which was confirmed to be due to the porous structure created by the interaction between the Gelatin/CMCS network and PEDOT: PSS. The formation of these pores allowed PEDOT: PSS to distribute more effectively, reinforcing electron-transport pathways and thereby enhancing electrical conductivity [42]. The porous structure also facilitated the absorption of electrolytes and promoted ion mobility [76], thereby increasing ionic conductivity. However, the continuity of the PEDOT: PSS network is critical to electrical conductivity. Therefore, the study demonstrated that the electrical conductivity of the GCP hydrogel can be effectively enhanced by adjusting the PEDOT: PSS concentration.

The electrochemical performance of GCP hydrogels with varying PEDOT: PSS content was evaluated by cyclic voltammetry (CV) in a three-electrode system. Conductive materials like PEDOT: PSS significantly influence cell adhesion and proliferation [77, 78]. As shown in Figure S5(c), the CV of GCP without PEDOT: PSS exhibited a relatively low redox peak current of 0.1 μA. In contrast, the GCP with PEDOT: PSS demonstrated a higher redox peak current of 0.29 μA, confirming the electrochemical activity of PEDOT: PSS within the hydrogel.

Figure S5(d) presents the CV curves of various GCP electrodes at a scan rate of 25 mV/s, showing improved charge storage performance with the addition of PEDOT: PSS compared to pure GCP_0, which displayed only 0.001 μA at the same scan rate. Additionally, Figure S5(e) shows the CV curves of GCP2 at scan rates ranging from 25 to 150 mV/s. The GCP_2 electrode maintained a wide potential window of −0.5 to 1.5 V, with all curves displaying symmetric shapes at increasing scan rates. This indicates excellent capacitive properties and stability.

Test results for mechanical and electrical properties indicate that PEDOT: PSS concentration affects the electrical characteristics of the GCP hydrogel. As the PEDOT: PSS concentration increased, its ionic conductivity gradually improved. Additionally, water content decreased with increasing PEDOT: PSS concentration.

Thermal stability analysis

The thermal stability of PCP/CUR electrospun fibers was analyzed to evaluate their processability and practical applicability. In particular, the decomposition behavior at high temperatures was examined to verify the material's stability and heat resistance [79]. Thermogravimetric analysis (TGA) results showed that PC electrospun fibers exhibited greater weight loss compared to PCP electrospun fibers containing PLA (Figure S3(e)). The decomposition temperatures of PC electrospun fibers were observed at 340 °C and 420 °C. In contrast, the decomposition temperature of PCP electrospun fibers was observed at 420 °C. The addition of PLA enhanced the thermal stability of the PCP/CUR electrospun fibers, as indicated by the TGA results.

In vitro CUR release study

The cumulative CUR release profile of PCP/CUR electrospun fibers in PBS (pH 7.4) is shown in Fig. 3(o). The highest CUR release was observed from the PCP/CUR-3 sample, with an initial rapid release followed by a sustained release over 48 h. The cumulative CUR release tended to increase with increasing CUR content in the PCP/CUR-1 and PCP/CUR-3 samples, which can be attributed to their higher CUR loading and relatively porous network structures. The release rate later became more controlled and sustained. The slow and steady CUR release from PCP/CUR suggests the occurrence of covalent interactions between CUR and the PCP surface. This sustained-release profile provides continuous therapeutic effects during the wound healing process by ensuring steady drug release over an extended period [80].

The ES promotes biocompatibility

Biocompatibility is a critical characteristic for applications in tissue engineering [81]. In this study, the biocompatibility and cell proliferation of HDF and HaCaT cells with PCP/CUR electrospun fiber and GCP hydrogel were evaluated using the WST-8 assay. As shown in Figs. 4(a, b), PCP/CUR electrospun fibers exhibited excellent cell viability compared to the untreated control group when cultured with HDF and HaCaT cells for 1, 3, and 7 days. Notably, on day 7, the PCP/CUR-1 and PCP/CUR-3 samples containing CUR showed the highest cell viability. The cell viability data were further confirmed with live/

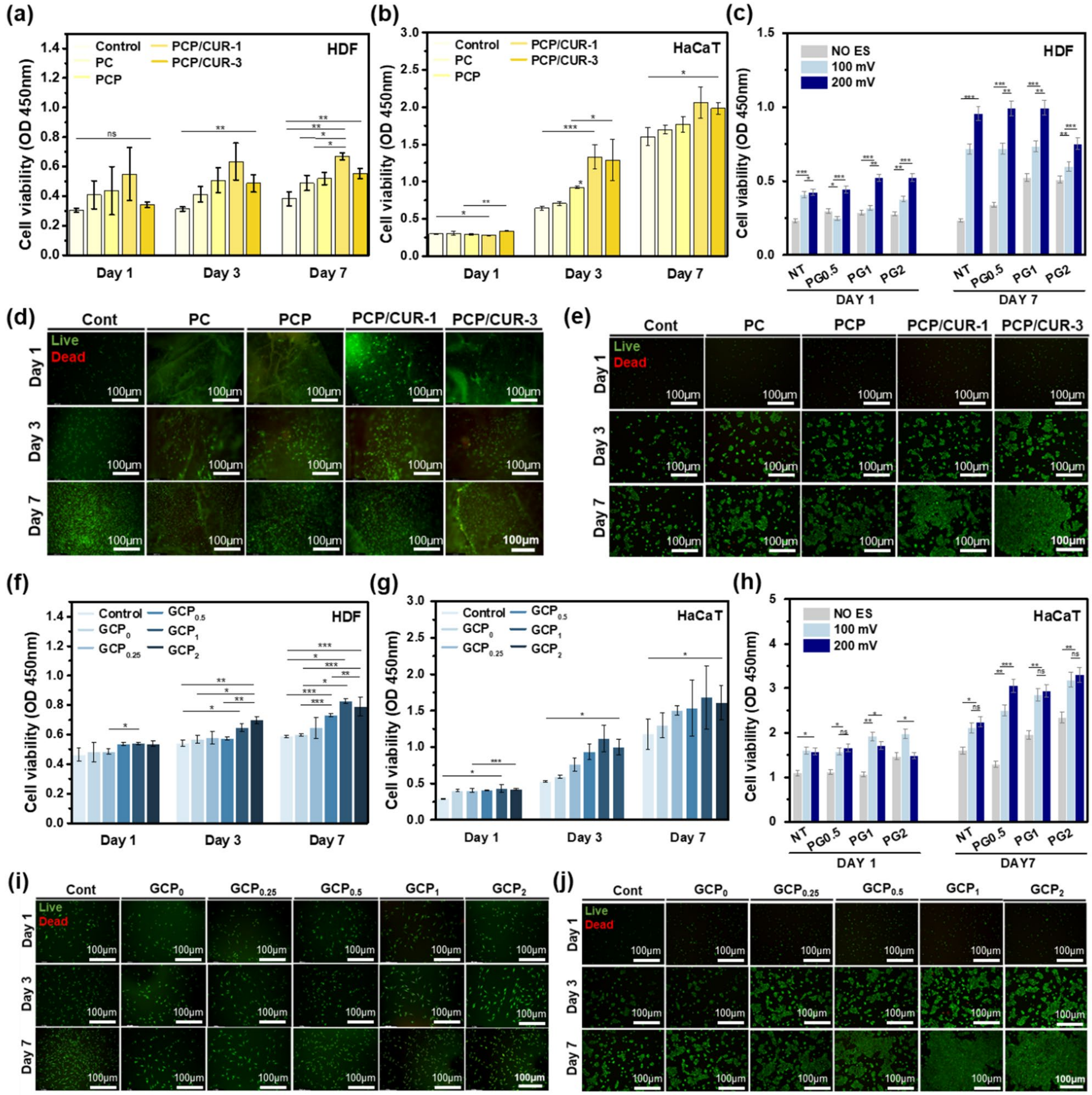

Fig. 4 Proliferation and viability of HDF and HaCaT cells with GCP hydrogels, PCP/CUR electrospun fibers, and ES treatment. **(a)** Cell viability of HDF cells cultured with PCP/CUR electrospun fibers over 1, 3, and 7 days. **(b)** Cell viability of HaCaT cells cultured with PCP/CUR electrospun fibers over 1, 3, and 7 days. **(c)** Cell viability assessment of HDF under various ES. **(d)** Proliferation of HDF cells cultured with PCP/CUR electrospun fibers for 1, 3, and 7 days. **(e)** Proliferation of HaCaT cells cultured with PCP/CUR electrospun fibers for 1, 3, and 7 days. **(f)** Cell viability of HDF cells cultured in GCP hydrogels over 1, 3, and 7 Days. **(g)** Cell viability of HaCaT cells cultured in GCP hydrogels over 1, 3, and 7 Days. **(h)** Cell viability assessment of HaCaT cells under various ES. **(i)** Proliferation of HDF cells after 7 days of culture with GCP hydrogels. **(j)** Proliferation of HaCaT cells after 7 days of culture with GCP hydrogels. Data are mean ± SD of triplicated experiments, statistical significance at $^{*}p < 0.05$, $^{**}p < 0.01$, and $^{***}p < 0.001$. Scale bar: 100 μm

dead assessment, and no dead cells were observed following treatment for 7 days with respective samples (Fig. 4(d, e), Figure S7(a, b)). Next, the cell compatibility of HDF and HaCaT cells with GCP hydrogel was investigated; the results revealed an enhanced cell viability trend as PEDOT: PSS concentration increased in the GCP hydrogel compared to the control group (Fig. 4(f, g), Figure S7(c, d)). These results collectively demonstrate that none of the prepared samples exhibited cytotoxicity and that they possess excellent in vitro biocompatibility. Figure 4(i, j) shows the cell viability of HDF and HaCaT cells cultured with GCP hydrogels. The fluorescent microscopy analysis confirmed that, as incubation time increased, both cell types proliferated, and the density of viable cells increased. Notably, the highest cell density was observed in GCP_1 and GCP_2, which contained higher PEDOT: PSS concentrations.

Additionally, compared to GCP_0, the release of PEDOT: PSS from the hydrogel did not hinder the growth of HDF and HaCaT cells. Therefore, the GCP hydrogels developed in this study exhibited no cytotoxicity and demonstrated excellent biocompatibility with HDF and HaCaT cells [11]. Following the biocompatibility evaluation of electrospun fibers and hydrogel individually, we next evaluated the effect of a combined hydrogel scaffold under various ES; the group without ES was considered the control, and 100 mV and 200 mV were applied to cells. The results suggested that HDF and HaCaT cells cultured at 200 mV exhibit higher cell viability than the control group (Fig. 4(c, h)). In the co-culture experiment of HDF and HaCaT cells, no cell death was observed, and cells exposed to 200 mV electrical stimulation showed higher viability compared to the control group(Figure S6(a)). These results indicate that the higher cell viability may result from the combined effect of PG hydrogel scaffolds and ES, allowing the cells to proliferate rapidly.

Effects of PG hydrogel scaffolds and ES on cell cytoskeleton arrangement and migration

To analyze the effects of PG hydrogel scaffolds and ES, cells' actin (F-actin), paxillin, and nuclei were visualized by immunostaining. The results showed that cells cultured under ES exhibit an aligned actin fiber arrangement. Moreover, the cells treated with the PG hydrogel scaffold, with and without ES, show higher fluorescence intensity of actin fibers (Fig. 5(a)). The cells also exhibited a significantly higher nuclear aspect ratio and a greater number of focal adhesion points than the non-ES groups. ES provides a signal that guides cell migration, known as electrotaxis. During this process, various cell types exhibit membrane protrusions and redistribution of active membrane receptor proteins, which have been reported to promote tissue regeneration [82, 83]. To further investigate the role of ES in cytoskeletal dynamics, the expression of actin (F-actin) was quantitatively analyzed using Corrected Total Cell Fluorescence (CTCF). In HDF cells, the actin expression in the ES-treated groups (PG1 + ES, PG2 + ES) was $2.04 \times 10^6 \pm 0.01 \times 10^6$, $1.57 \times 10^6 \pm 0.01 \times 10^6$, which was higher compared to the non-ES groups (PG1-ES, PG2-ES) with $1.76 \times 10^6 \pm 0.14 \times 10^6$, $1.39 \times 10^6 \pm 0.14 \times 10^6$ (Fig. 5(b)). Similarly, in HaCaT cells, the actin expression in the PG2 + ES group was $5.57 \times 10^6 \pm 0.15 \times 10^6$, while the PG2-ES group had $4.56 \times 10^6 \pm 0.14 \times 10^6$, showing a significant increase in the ES-treated group (Fig. 5(c)). This suggests that the combination of ES and PG2 scaffold structure provides optimal conditions for cytoskeletal organization and cellular activity, further supporting the idea that ES plays a crucial role in promoting cell polarity and structural integrity.

We further investigated the mechanism of wound healing induced by PG hydrogel scaffolds combined with ES through in vitro experiments, focusing on cell adhesion and migration. To simulate wound closure, we employed an in vitro scratch assay to study the effects of ES on cell adhesion and migration. After 48 h of culture and ES, wound closure was significantly accelerated in the ES-treated groups (Fig. 5(d)). Compared to the non-ES groups, the wound closure rate in HDF cells was approximately 1.5 to 1.8 times higher, and in HaCaT cells, it was 1.1 to 1.3 times higher (Fig. 5(e, f). Significant differences were observed between the NT + ES, PG1 + ES, and PG2 + ES groups. The faster wound closure observed in the PG1 + ES and PG2 + ES groups could be attributed to the combined effects of PCP/CUR and GCP in promoting cell adhesion, as well as ES enhancing cell migration. The applied EF can influence directional cell movement, promoting active behavior associated with cell growth rather than passive swimming under its influence. The ability of ES to promote cell migration, combined with the adhesion-enhancing effects of PCP/CUR and GCP, significantly accelerated wound closure. This suggests that the combination of PG hydrogel scaffolds and ES effectively promotes skin healing at the cellular level.

ES promotes the ROS generation

ROS plays a significant role in promoting antibacterial properties, and a moderate level also supports cell migration. To evaluate the effect of ES on ROS production, DCF-DA staining and a DPPH assay were performed. The group without H_2O_2 (-/+) ES was considered the negative control group, and the group with + H_2O_2 (-/+) ES was considered the positive treatment group. Upon DCF-DA assay, the cells in the - H_2O_2 (-/+) ES show a baseline fluorescent intensity, while the + H_2O_2 (-/+) ES show increased fluorescent intensity (Figure S8(a)). Among those, the PG1 hydrogel scaffold + ES (+ H2O2) exhibits higher fluorescence, supporting the production of ROS

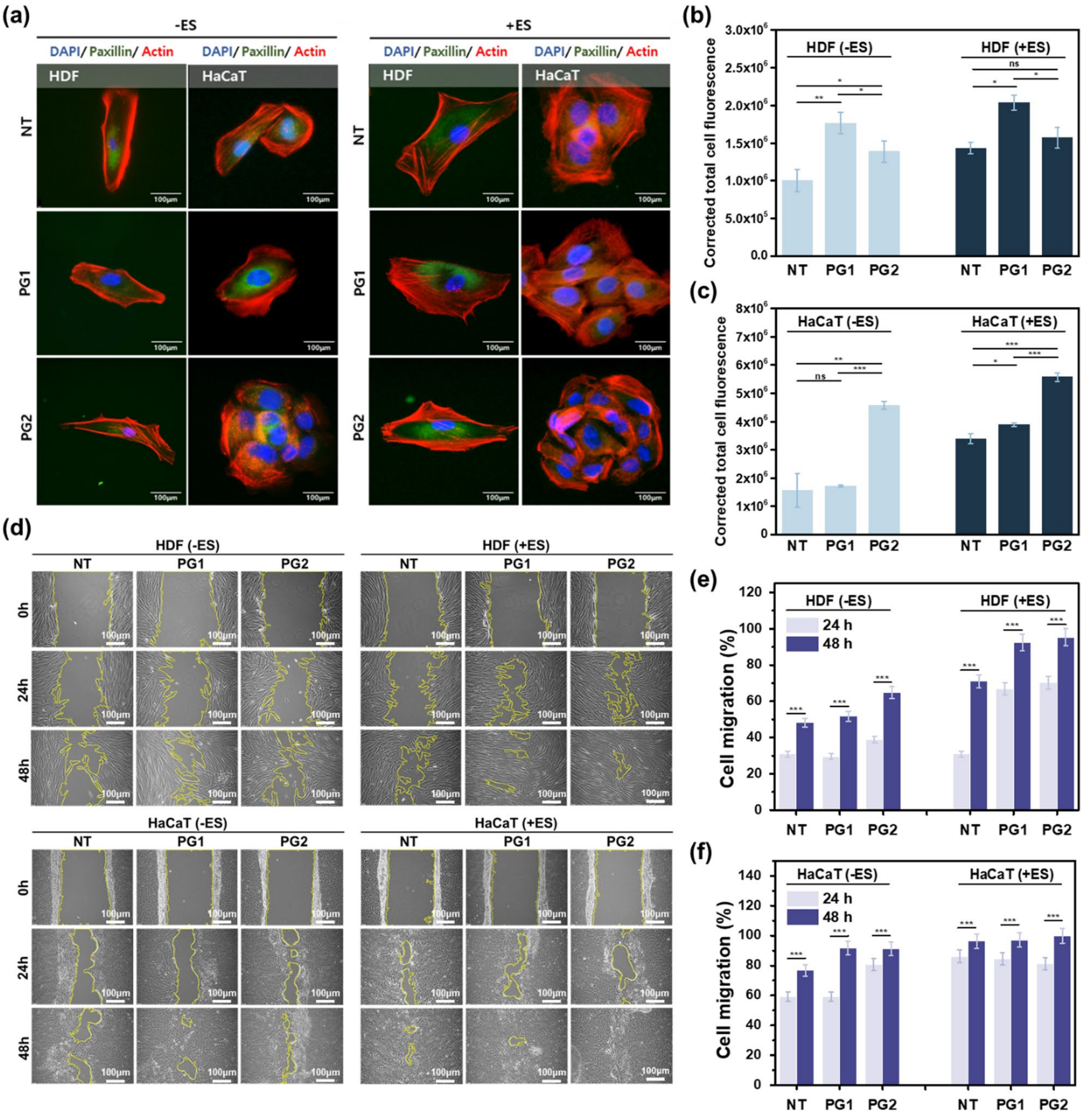

Fig. 5 Effects of ES-treated PG hydrogel scaffolds on HDF and HaCaT cells. **(a)** Immunofluorescence staining of HDF and HaCaT cells, in the presence of ES-treated PG hydrogel scaffolds, showing the focal adhesion points (Paxillin; green), cytoskeleton (F-actin; red), and nucleus (DAPI; blue) after 7 days of culture (HDF, left; HaCaT, 7, right). Scale bar: 100 µm. **(b)** CTCF of actin expression in HDF cells on PG hydrogel scaffolds. **(c)** CTCF of actin expression in HaCaT cells on PG hydrogel scaffolds. **(d)** Representative images showing wound closure after 48 h of ES treatment. Scale bar: 100 µm. **(e, f)** Quantification of cell migration in HDF and HaCaT cells, showing a significant acceleration of closure in ES-treated groups compared to non-ES groups. Data are mean ± SD of triplicated experiments, statistical significance at $*p < 0.05$, $**p < 0.01$, and $***p < 0.001$. Scale bar: 100 µm

in the presence of ES. Additionally, the DPPH assay used to measure antioxidant activity revealed that the hydrogel scaffolds PG1 and PG2 (-/+ES) showed reduced DPPH activity compared to the control groups and PCL samples (Figure S8(b)). These results indicate that in the presence of ES, ROS activity enhances due to the ES responsiveness of the samples (PG1 and PG2), leading to the antibacterial effects of the hydrogel scaffolds.

Effect of PG hydrogel scaffolds with ES on the expression of genes related to tissue repair

To further investigate the efficacy of PG hydrogel scaffolds and ES in wound healing, we analyzed gene expression of wound healing genes, such as fibronectin and collagen, as well as apoptosis-related genes, including *Bcl2*, *P53*, and *Bax*. In HDF cells, gene expression changes following ES were as follows (Fig. 6(a-e)). Fibronectin and collagen expression were significantly increased in the PG2 + ES group compared to the non-stimulated control group, indicating that ES promoted the synthesis of fibronectin and collagen, which are important for ECM generation and wound healing [84]. Furthermore, to analyze the effect of ES on apoptosis, we examined the expression of *Bcl2* (anti-apoptotic gene), *P53*, and *Bax* (pro-apoptotic genes). The results showed that Bcl_2 expression was increased in the ES-treated groups, whereas Bax and P53 expression were significantly decreased, indicating that ES promotes cell survival and inhibits apoptosis.

Similarly, changes in gene expression due to ES treatment in HaCaT cells followed a similar trend (Fig. 6(f-k)). Keratin-related genes such as *KRT1*, *KRT10*, and *KRT14* were upregulated in the ES-treated groups [85, 86], suggesting that ES facilitates keratinocyte differentiation. Additionally, the expression of *Bax* and *P53* showed a decreasing trend, further indicating that ES contributes to the regulation of cell survival. These results demonstrate that ES has a significant effect on cellular regulatory mechanisms related to the cell cycle [87]. Overall, the PG2 + ES group showed the greatest enhancement in tissue repair-related gene expression.

To validate the gene expression data, we assessed fibronectin protein expression by immunocytochemistry. Fibronectin expression showed a clear difference between ES. In HDF cells, the ES-treated groups (PG1 + ES: $1.38 \times 10^6 \pm 0.03 \times 10^6$, PG2 + ES: $0.98 \times 10^5 \pm 0.2 \times 10^5$) exhibited significantly higher fibronectin expression compared to the non-treated groups (PG1-ES: $8.5 \times 10^5 \pm 0.26 \times 10^5$, PG2-ES: $1.22 \times 10^6 \pm 0.01 \times 10^6$) (Fig. 6(l), S6(b)).

The PG hydrogel scaffold exhibits higher antibacterial properties

Damaged skin loses its barrier function, which protects the host from pathogens [88]. In addition, exudates and proteins from ischemic necrotic tissue can lead to bacterial infections, delay wound healing, and increase exudates and improper collagen accumulation [89]. Therefore, excellent antibacterial properties are an important characteristic of high-quality wound dressings [90, 91]. CUR exhibits antibacterial properties against both Gram-positive and Gram-negative bacteria without inducing drug resistance [92]. ES plays a crucial role in inhibiting and disrupting bacteria and biofilm formation by generating ROS and H_2O_2. This process prevents infection, promoting wound healing and tissue regeneration simultaneously.

For this, the antibacterial efficacy of CUR was activated by applying ES to the PG hydrogel scaffolds, inhibiting bacterial attachment and growth (Fig. 7(a)). Before applying ES, antibacterial experiments were conducted using *E. coli.* The optical density measurement showed that the PCP/CUR electrospun fibers with CUR exhibited superior antibacterial properties compared to the control group, with the highest antibacterial efficacy observed in the PCP/CUR-3 group (Fig. 7(b)). Based on these results, PCP/CUR-3 was used as the outer layer of the PG hydrogel scaffold in subsequent antibacterial experiments.

To investigate the antibacterial properties of the combined PG hydrogel scaffolds in the presence of ES, *E. coli* and MRSA were used, and tetracycline (TC) was employed as a positive control group. The results showed that the proliferation rates of both *E. coli* and MRSA significantly decreased after the addition of 3% CUR and ES, with a higher inhibition rate against MRSA than *E. coli*. Moreover, the antibacterial effect of the PG hydrogel scaffolds increased with higher concentrations of PEDOT: PSS and CUR, particularly showing the highest antibacterial efficacy in the PG2 + ES group (Fig. 7(c, d)). Plating analysis was performed to assess bacterial survival and colony formation, as shown in Fig. 7(e), the number of colonies of both bacterial species was significantly reduced in the ES-treated groups compared to the non-ES groups (Fig. 7(f, g)).

Biofilm formation is one of the major bacterial mechanisms that interfere with the effectiveness of antibiotic treatment [93]. Disrupting biofilms has the potential to enhance the antibacterial effect. After 48 h of biofilm formation, the efficacy of PG + ES was evaluated (Fig. 7(h)). Both PG-ES and PG + ES scaffolds demonstrated biofilm disruption effects against *E. coli* and MRSA compared to the control group, with PG2 + ES showing superior biofilm destruction.

In conclusion, the results of this study suggest that the PG + ES scaffold can be utilized as a nanocomposite material with strong antibacterial potential against biofilms in the wound healing process.

Conclusion

The PG hydrogel scaffold developed in this study successfully replicated the multiscale architecture of natural skin by integrating the upper PCP/CUR electrospun fiber layer with the lower 3D printed GCP hydrogel layer. The electrospun fiber diameters (ranging from 5 to 34 μm) and hydrogel pore sizes (ranging from 65 to 202 μm) corresponded to the microstructural features of the collagen fiber network and dermal ECM, respectively, while the cross-hatch printing pattern provided ECM-like anisotropy [94, 95]. Such morphological biomimicry played a crucial role in enhancing cell adhesion, migration, and proliferation, as well as improving wound regeneration

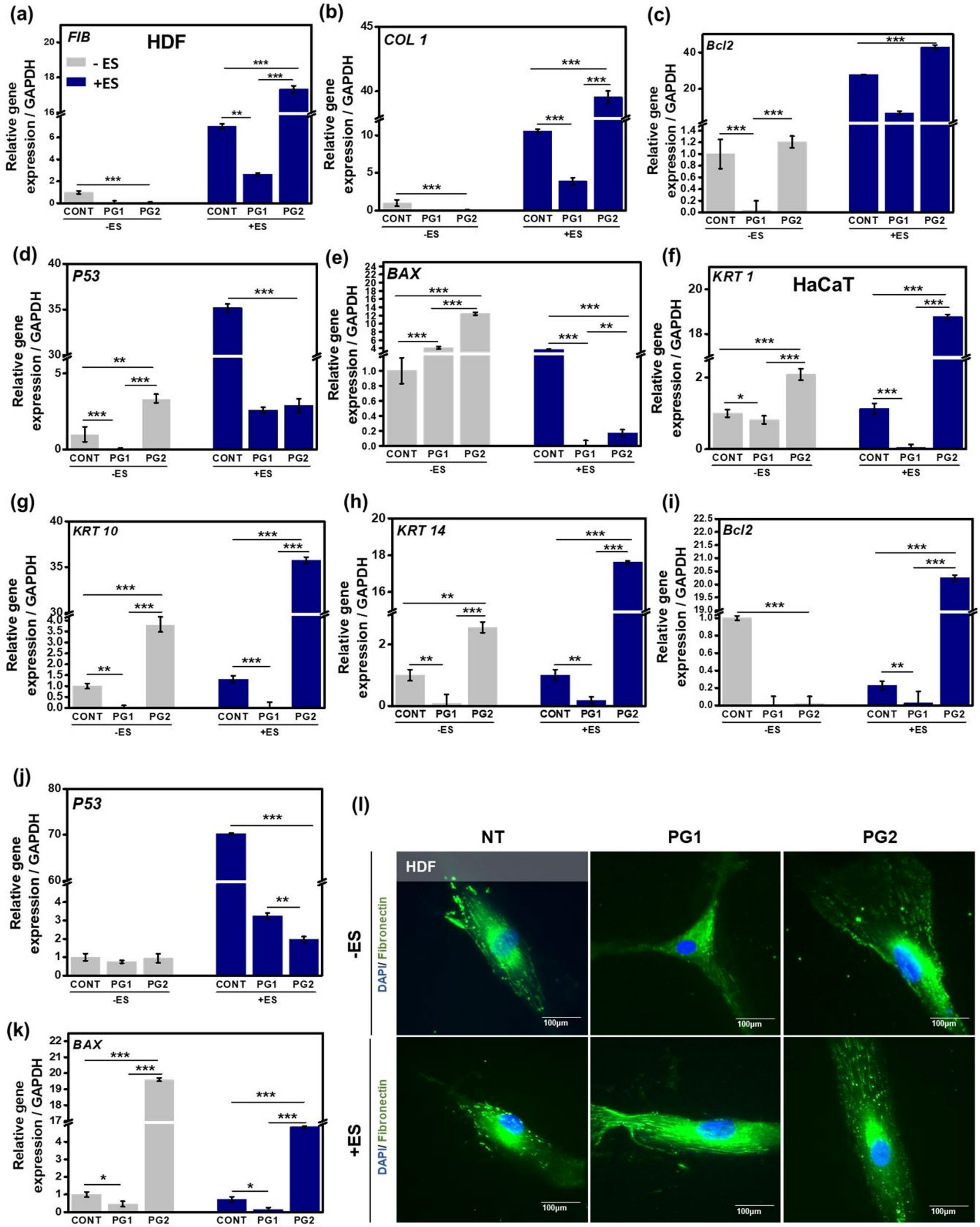

Fig. 6 Gene expression changes in HDF and HaCaT cells treated with ES. **(a-e)** Gene expression changes in HDF cells : **(a)** Fibronectin **(b)***COL1* **(c)***P53* **(d)***BAX* **(e-i)** Gene expression changes in HaCaT cells: **(e)***KRT1* **(f)***KRT10* **()***KRT14* **(i)***Bcl2* **(j)***P53* **(k)***BAX*. **(l)** Fibronectin expression in HDF cells. Data are mean ± SD of triplicated experiments, statistical significance at *$p < 0.05$, **$p < 0.01$, and ***$p < 0.001$. Scale bar: 100 μm

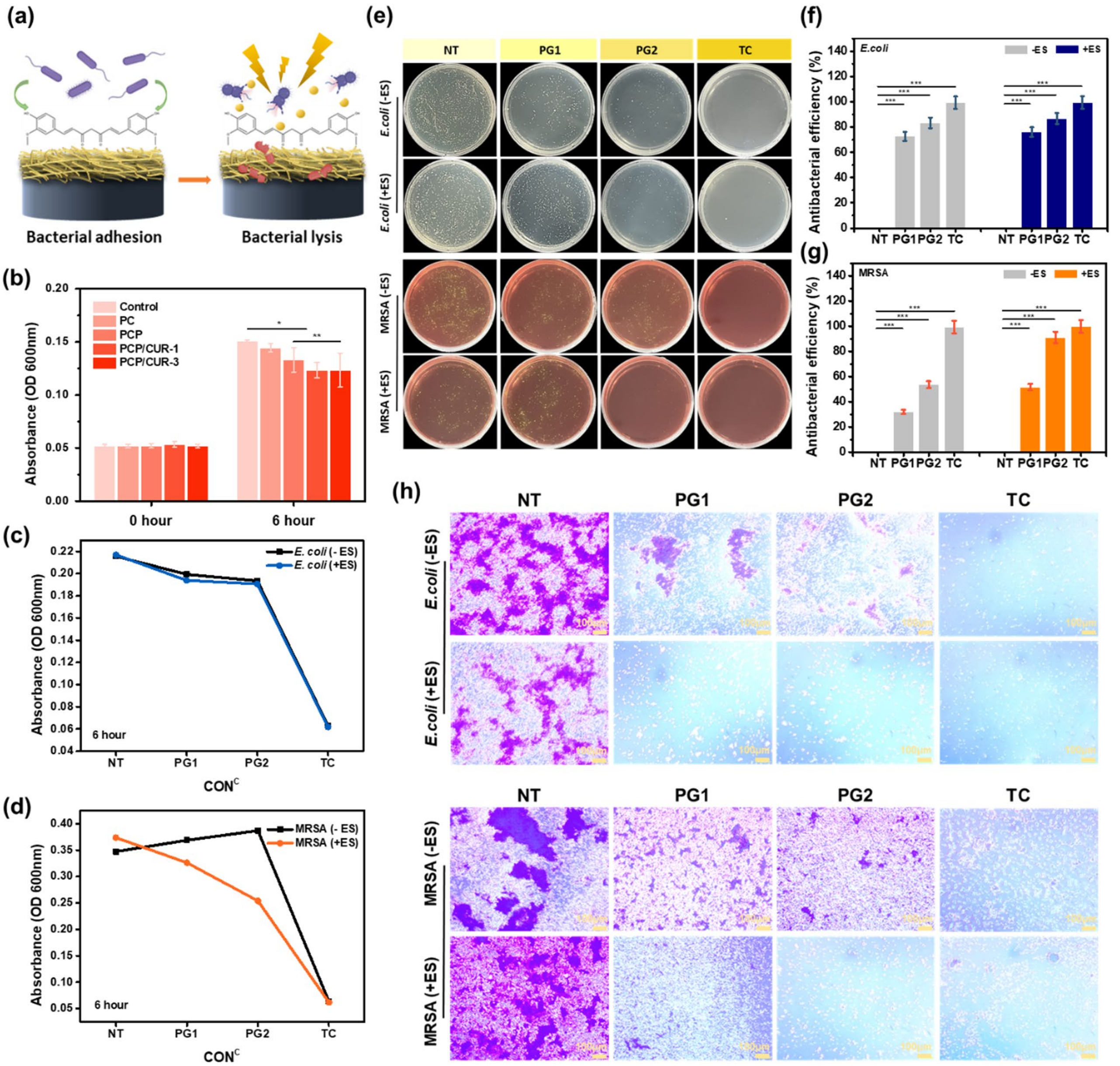

Fig. 7 Antibacterial efficacy of PG hydrogel scaffolds with CUR and ES. **(a)** Activation of CUR antibacterial properties through ES on PG hydrogel scaffolds, inhibiting bacterial attachment and growth. **(b)** Antibacterial activity of PCP/CUR electrospun fibers tested against *E. coli*, showing superior efficacy in PCP/CUR-3. **(c, d)** Inhibition of *E. coli* and MRSA proliferation after 3% CUR addition and ES, with enhanced antibacterial effects in PG2 + ES. **(e)** Colony formation analysis demonstrating significant reduction in bacterial colonies under ES and their **(f, g)** Antibacterial efficiency percentage. **(h)** Biofilm disruption effect of PG-ES and PG + ES scaffolds against *E. coli* and MRSA, with PG + ES showing superior biofilm destruction. Data are mean ± SD of triplicated experiments, statistical significance at $*p < 0.05$, $**p < 0.01$, and $***p < 0.001$. Scale bar: 100 µm

through ES responsiveness. Therefore, the PG hydrogel scaffold demonstrated excellent potential as a morphologically and functionally biomimetic conductive platform for wound healing applications. A comparative table of various conductive scaffolds used in the field of tissue engineering is presented in Table S3. The drug release study showed sustained CUR release from PCP/CUR electrospun fibers over 48 h, supporting the long-term antibacterial and therapeutic effects of the PG hydrogel scaffold.

This study demonstrates that PG hydrogel scaffolds combined with ES effectively promote wound healing. The incorporation of PEDOT: PSS into GCP hydrogels enhanced cell proliferation and adhesion, while CUR-loaded PCP/CUR electrospun fibers exhibited strong antibacterial activity against *E. coli* and MRSA, including effective biofilm inhibition. Additionally, ROS assay results showed that PG hydrogel scaffolds, especially when combined with ES, significantl produced intracellular ROS levels in HDF cells under H_2O_2-induced oxidative stress, indicating effective protection against bacterial damage. These results indicate that the designed materials are well suited for wound healing applications and can simultaneously address two major challenges in chronic wounds: infection and impaired tissue regeneration.

ES applied at 25 Hz and 200 mV further stimulated cell proliferation, directional migration (electrotaxis), and in vitro wound closure. The effect was particularly pronounced in PG hydrogel scaffolds, where the structured hydrogel surface facilitated cell attachment, ECM synthesis, and cell survival, creating a favorable microenvironment for tissue regeneration. The combination of CUR and ES synergistically enhanced antibacterial efficacy, resulting in greater inhibition of bacterial growth and biofilm formation compared to scaffolds or ES alone. Moreover, PG hydrogel scaffolds with ES significantly upregulated wound healing–related proteins, including fibronectin, collagen, and keratins, supporting both cellular activity and functional tissue development. The PG hydrogel scaffolds maintained high biocompatibility with minimal cytotoxicity in HDF and HaCaT cells, further highlighting their safety and potential for clinical application. Compared with conventional hydrogel or electrospun fiber treatments, the PG hydrogel scaffold system offers distinct advantages by integrating structural support, ES, and antibacterial activity. Although in vitro results are promising, further in vivo studies are needed to validate long-term efficacy and biocompatibility under more complex physiological conditions. Optimization of ES parameters and scaffold composition may further enhance therapeutic outcomes.

In conclusion, PG hydrogel scaffolds combined with ES represent a promising platform for the treatment of chronic and infected wounds. By simultaneously promoting cell activity, facilitating tissue regeneration, and preventing bacterial infection, this approach addresses key limitations of current therapies and highlights its translational potential to improve clinical outcomes.

Abbreviations

PEDOT: PSS	Poly (3,4-ethylenedioxythiophene): poly (styrenesulfonate)
CS	Chitosan
CMCS	Carboxymethyl chitosan
ES	Electrical stimulation
DC	Direct-current
hBMSCs	human bone marrow-derived mesenchymal stem cells
ECM	Extracellular matrix
ROS	Reactive oxygen species
H_2O_2	Hydrogen peroxide
DMF	N, N-dimethylformamide
DCM	Dichloromethane
PCL	Polycaprolactone
PLA	Polylactic acid
CUR	Curcumin
MRSA	Methicillin-resistant*Staphylococcus aureus*
E. coli	*Escherichia coli*
HDF	Human dermal fibroblast
HaCaT	Human keratinocyte
CV	Cyclic voltammetry
GCE	Glassy carbon electrode
SEM	Scanning Electron Microscopy
Pt	Platinum
EDS	Energy Dispersive X-ray Spectroscopy
XPS	X-ray Photoelectron Spectroscopy
FTIR	Fourier-transform infrared
NB	Nutrient Broth
CFU	Colony-forming unit
PFA	Paraformaldehyde
EF	Electric field
AF	Alexa Fluor
CTCF	Corrected total cell fluorescence
DCF-DA	Dichlorodihydrofluorescein diacetate
DPPH	2, 2-diphenyl-2-picrylhydrazyl
CFU	Colony-forming unit
PBS	Phosphate-buffered saline
GAPDH	Glyceraldehyde 3-phosphate dehydrogenase
FN	Fibronectin
Col1	Collagen 1
BAX	BCL2-associated X protein
P53	tumor protein p53
BCL2	B-cell leukemia/lymphoma 2
KRT 1	Keratin 1
Keratin 5	Keratin 5
KRT 10	Keratin 10
KRT 14	Keratin 14

Supplementary Information

The online version contains supplementary material available at https://doi.org/10.1186/s12951-025-03938-2.

Supplementary Material 1

Acknowledgements
Not applicable.

Author contributions
Writing-Original draft; J.L., Conceptualization; J.L.; Methodology; J.L., H.P., H.K.; Formal analysis, validation, investigation; A. R., Data curation, software: J. L., and A. R.; Writing-Review & Editing: J. L., and A. R.; Visualization, Supervision: K.T.L., and A. R.; Project administration, Funding acquisition: K.T.L.; S.J.C.

Funding
This study was supported by the 'Basic Science Research Program' through the 'National Research Foundation of Korea' funded by the 'Ministry of Education' (RS-2025-16065692; RS-2023-00245155; RS-2018-NR031068). This work was supported by Innovative Human Resource Development for Local Intellectualization program through the Institute of Information & Communications Technology Planning & Evaluation (IITP) grant funded by the Korea government (RS-2023-00260267).

Data availability
The dataset used and/or analysed dueing the current study are available from the corresponding author on reasonable request.

Declarations

Ethics approval and consent to participate
Not applicable.

Consent for publication
Not applicable.

Competing interests

The authors declare no competing interests.

Author details

[1]Department of Biosystems Engineering, Kangwon National University, Chuncheon 24341, Republic of Korea
[2]Interdisciplinary Program in Smart Agriculture, Kangwon National University, Chuncheon 24341, Republic of Korea
[3]Department of Food Science and Biotechnology, Kangwon National University, Chuncheon 24341, Republic of Korea

Received: 20 August 2025 / Accepted: 10 December 2025

References

1. Peña OA, Martin P. Cellular and molecular mechanisms of skin wound healing. Nat Rev Mol Cell Biol. 2024:1–18.
2. Wang G, Yang F, Zhou W, Xiao N, Luo M, Tang Z. The initiation of oxidative stress and therapeutic strategies in wound healing. Biomed Pharmacother. 2023;157: 114004.
3. Fu W, Sun S, Cheng Y, Ma J, Hu Y, Yang Z, et al. Opportunities and challenges of nanomaterials in wound healing: advances, mechanisms, and perspectives. Chem Eng J. 2024. https://doi.org/10.1016/j.cej.2024.153640.
4. Cavallo I, Sivori F, Mastrofrancesco A, Abril E, Pontone M, Di Domenico EG, et al. Bacterial biofilm in chronic wounds and possible therapeutic approaches. Biology. 2024;13(2):109.
5. Cullen B, Gefen A. The biological and physiological impact of the performance of wound dressings. Int Wound J. 2023;20(4):1292–303.
6. Freedman BR, Hwang C, Talbot S, Hibler B, Matoori S, Mooney DJ. Breakthrough treatments for accelerated wound healing. Sci Adv. 2023;9(20):eade7007.
7. Alavi SE, Alavi SZ, Nisa MU, Koohi M, Raza A, Ebrahimi Shahmabadi H. Revolutionizing wound healing: exploring scarless solutions through drug delivery innovations. Mol Pharm. 2024;21(3):1056–76.
8. Cai Y, Chen K, Liu C, Qu X. Harnessing strategies for enhancing diabetic wound healing from the perspective of spatial inflammation patterns. Bioact Mater. 2023;28:243–54.
9. Zhang X, Wang T, Zhang Z, Liu H, Li L, Wang A, et al. Electrical stimulation system based on electroactive biomaterials for bone tissue engineering. Mater Today. 2023. https://doi.org/10.1016/j.mattod.2023.06.011.
10. Huang Y, Yao K, Zhang Q, Huang X, Chen Z, Zhou Y, et al. Bioelectronics for electrical stimulation: materials, devices and biomedical applications. Chem Soc Rev. 2024. https://doi.org/10.1039/D4CS00413B.
11. Preetam S, Ghosh A, Mishra R, Pandey A, Roy DS, Rustagi S, et al. Electrical stimulation: a novel therapeutic strategy to heal biological wounds. RSC Adv. 2024;14(44):32142–73.
12. Das KK, Basu B, Maiti P, Dubey AK. Interplay of piezoelectricity and electrical stimulation in tissue engineering and regenerative medicine. Appl Mater Today. 2024;39:102332.
13. Hamid S, Hayek R. Role of electrical stimulation for rehabilitation and regeneration after spinal cord injury: an overview. Eur Spine J. 2008;17:1256–69.
14. Tyler SE. Nature's electric potential: a systematic review of the role of bioelectricity in wound healing and regenerative processes in animals, humans, and plants. Front Physiol. 2017;8:627.
15. Ennis WJ, Lee C, Gellada K, Corbiere TF, Koh TJ. Advanced technologies to improve wound healing: electrical stimulation, vibration therapy, and ultrasound—what is the evidence? Plast Reconstr Surg. 2016;138(3S):94S-104S.
16. Tai G, Tai M, Zhao M. Electrically stimulated cell migration and its contribution to wound healing. Burns Trauma. 2018;6:20.
17. Park HJ, Rouabhia M, Lavertu D, Zhang Z. Electrical stimulation modulates the expression of multiple wound healing genes in primary human dermal fibroblasts. Tissue Eng Part A. 2015;21(13–14):1982–90.
18. Ud-Din S, Bayat A, editors. Electrical stimulation and cutaneous wound healing: a review of clinical evidence. Healthcare: MDPI; 2014.
19. Stojanovic M, Rai V, Agrawal DK. Effect of electromagnetic field on proliferation and migration of fibroblasts and keratinocytes: implications in wound healing and regeneration. J Biotechnol Biomed. 2024;7(3):387.
20. Dutta SD, Ganguly K, Randhawa A, Patil TV, Patel DK, Lim K-T. Electrically stimulated 3D bioprinting of gelatin-polypyrrole hydrogel with dynamic semi-IPN network induces osteogenesis via collective signaling and immunopolarization. Biomaterials. 2023;294:121999.
21. Veith AP, Henderson K, Spencer A, Sligar AD, Baker AB. Therapeutic strategies for enhancing angiogenesis in wound healing. Adv Drug Deliv Rev. 2019;146:97–125.
22. Niu Y, Li Q, Ding Y, Dong L, Wang C. Engineered delivery strategies for enhanced control of growth factor activities in wound healing. Adv Drug Deliv Rev. 2019;146:190–208.
23. Lai H-J, Kuan C-H, Wu H-C, Tsai J-C, Chen T-M, Hsieh D-J, et al. Tailored design of electrospun composite nanofibers with staged release of multiple angiogenic growth factors for chronic wound healing. Acta Biomater. 2014;10(10):4156–66.
24. Bai Q, Zheng C, Chen W, Sun N, Gao Q, Liu J, et al. Current challenges and future applications of antibacterial nanomaterials and chitosan hydrogel in burn wound healing. Mater Adv. 2022;3(17):6707–27.
25. Wang Y, Zhang M, Yan Z, Ji S, Xiao S, Gao J. Metal nanoparticle hybrid hydrogels: the state-of-the-art of combining hard and soft materials to promote wound healing. Theranostics. 2024;14(4):1534.
26. Nie L, Wei Q, Li J, Deng Y, He X, Gao X, et al. Fabrication and desired properties of conductive hydrogel dressings for wound healing. RSC Adv. 2023;13(13):8502–22.
27. Cao Y, Sun J, Qin S, Zhou Z, Xu Y, Liu C. Advances and challenges in immune-modulatory biomaterials for wound healing applications. Pharmaceutics. 2024;16(8):990.
28. Chen S, Li R, Li X, Xie J. Electrospinning: an enabling nanotechnology platform for drug delivery and regenerative medicine. Adv Drug Deliv Rev. 2018;132:188–213.
29. Boekema BK, Vlig M, Olde Damink L, Middelkoop E, Eummelen L, Bühren AV, et al. Effect of pore size and cross-linking of a novel collagen-elastin dermal substitute on wound healing. J Mater Sci Mater Med. 2014;25(2):423–33.
30. Luo P, Nie M, Wen H, Xu W, Fan L, Cao Q. Preparation and characterization of carboxymethyl Chitosan sulfate/oxidized Konjac glucomannan hydrogels. Int J Biol Macromol. 2018;113:1024–31.
31. Patil TV, Dutta SD, Patel DK, Ganguly K, Lim K-T. Electrospinning near infra-red light-responsive unzipped CNT/PDA nanofibrous membrane for enhanced antibacterial effect and rapid drug release. Appl Surf Sci. 2023;612:155949.
32. Bui HT, Chung OH, Dela Cruz J, Park JS. Fabrication and characterization of electrospun curcumin-loaded polycaprolactone-polyethylene glycol nanofibers for enhanced wound healing. Macromol Res. 2014;22:1288–96.
33. Wang C, Ma C, Wu Z, Liang H, Yan P, Song J, et al. Enhanced bioavailability and anticancer effect of curcumin-loaded electrospun nanofiber: in vitro and in vivo study. Nanoscale Res Lett. 2015;10:1–10.
34. Cheng T, Wang F, Zhang Y-Z, Li L, Gao S-Y, Yang X-L, et al. 3D printable conductive polymer hydrogels with ultra-high conductivity and superior stretchability for free-standing elastic all-gel supercapacitors. Chem Eng J. 2022;450:138311.
35. Xie X, Xu Z, Yu X, Jiang H, Li H, Feng W. Liquid-in-liquid printing of 3D and mechanically tunable conductive hydrogels. Nat Commun. 2023;14(1):4289.
36. Wang Y, Zhou X, Jiang J, Zhao T, Dang J, Hu R et al. Carboxymethyl chitosan-enhanced multi-level microstructured composite hydrogel scaffolds for bone defect repair. Carbohydr Polym. 2024;348:122847.
37. Dey K, Roca E, Ramorino G, Sartore L. Progress in the mechanical modulation of cell functions in tissue engineering. Biomater Sci. 2020;8(24):7033–81.
38. Shariatzadeh FJ, Currie S, Logsetty S, Spiwak R, Liu S. Enhancing wound healing and minimizing scarring: A comprehensive review of nanofiber technology in wound dressings. Prog Mater Sci. 2024;147:101350.
39. Yang X, Cao L, Wang J, Chen L. Sandwich-like polypyrrole/reduced graphene oxide nanosheets integrated gelatin hydrogel as mechanically and thermally sensitive skinlike bioelectronics. ACS Sustain Chem Eng. 2020;8(29):10726–39.
40. Olanipekun EO, Ayodele O, Olatunde OC, Olusegun SJ. Comparative studies of chitosan and carboxymethyl chitosan doped with nickel and copper: characterization and antibacterial potential. Int J Biol Macromol. 2021;183:1971–7.
41. Zhang R, Wang Y, Li J, Zhao H, Wang Y, Zhou Y. Mesoporous cellulose nanofibers-interlaced PEDOT: PSS hybrids for chemiresistive ammonia detection. Microchim Acta. 2022;189(8):308.
42. Wang Y, Qu Z, Wang W, Yu D. PVA/CMC/PEDOT: PSS mixture hydrogels with high response and low impedance electronic signals for ECG monitoring. Colloids Surf B Biointerfaces. 2021;208:112088.
43. Qiao D, Li J, Zhang S, Yang X. Controlled release fertilizer with temperature-responsive behavior coated using polyether polyol (PPG)/polycaprolactone (PCL) blend-based polyurethane performs smart nutrient release. Mater Today Chem. 2022;26:101249.

44. Marcott C, Kansiz M, Dillon E, Cook D, Mang MN, Noda I. Two-dimensional correlation analysis of highly spatially resolved simultaneous IR and Raman spectral imaging of bioplastics composite using optical photothermal Infrared and Raman spectroscopy. J Mol Struct. 2020;1210:128045.
45. Sharma D, Satapathy BK. Understanding release kinetics and collapse proof suture retention response of curcumin loaded electrospun mats based on aliphatic polyesters and their blends. J Mech Behav Biomed Mater. 2021;120:104556.
46. Zou Y, Zhang C, Wang P, Zhang Y, Zhang H. Electrospun chitosan/polycaprolactone nanofibers containing chlorogenic acid-loaded halloysite nanotube for active food packaging. Carbohydr Polym. 2020;247:116711.
47. Karunarathne T, Sandaruwan C, Wijesinghe W, Karalasignham A, Abdelkader AM, Amaratunga G, et al. Development of universal fabric dyeing and adhesion through RF glow discharge plasma treatment. Vacuum. 2022;204:111394.
48. Sudhakar K, Suneetha M, Rao KM, Han SS. Antibacterial reduced graphene oxide reinforces polyelectrolyte hydrogels with polysaccharides via a green method. Colloids Surf A. 2021;628:127340.
49. Rashid F, Soshi SS, Gafur MA. Studies of XRD and FTIR on synthesized novel hybrid thin film made of Hydroxyapatite, Poly vinyl alcohol and gelatin for biomedical application. Mater Sci Appl. 2024;15(9):336–49.
50. Huang G, Liu G, Xu Z, Jiang L, Zhang Y, Sui X. Stability, rheological behavior and microstructure of Pickering emulsions co-stabilized by soy protein and carboxymethyl chitosan. Food Hydrocoll. 2023;142:108773.
51. Lee S, Kim J, Kim H, Kim C, Kim S, Kim C, et al. Brightening deep-blue perovskite light-emitting diodes: A path to Rec. 2020. Sci Adv. 2024;10(20):eadn8465.
52. Dodda JM, Azar MG, Bělský P, Šlouf M, Brož A, Bačáková L, et al. Biocompatible hydrogels based on chitosan, cellulose/starch, PVA and PEDOT: PSS with high flexibility and high mechanical strength. Cellulose. 2022;29(12):6697–717.
53. Furlani F, Montanari M, Sangiorgi N, Saracino E, Campodoni E, Sanson A, et al. Electroconductive and injectable hydrogels based on gelatin and PEDOT: PSS for a minimally invasive approach in nervous tissue regeneration. Biomaterials Sci. 2022;10(8):2040–53.
54. Sharma D, Satapathy BK. Physicomechanical performance and encapsulation efficiency of β-cyclodextrin loaded functional electrospun mats based on aliphatic polyesters and their blends. J Biomater Sci Polym Ed. 2021;32(11):1489–513.
55. Wasana PWD, Vajragupta O, Rojsitthisak P, Towiwat P, Rojsitthisak P. Metformin and Curcumin co-encapsulated chitosan/alginate nanoparticles as effective oral carriers against pain-like behaviors in mice. Int J Pharm. 2023;640:123037.
56. Haroosh HJ, Dong Y, Lau K-T. Tetracycline hydrochloride (TCH)-loaded drug carrier based on PLA: PCL nanofibre mats: experimental characterisation and release kinetics modelling. J Mater Sci. 2014;49:6270–81.
57. Kim N, Kee S, Lee SH, Lee BH, Kahng YH, Jo YR, et al. Highly conductive PEDOT: PSS nanofibrils induced by solution-processed crystallization. Adv Mater. 2014;26(14):2268–72.
58. Wen Y, Xu J. Scientific importance of water-processable PEDOT–PSS and preparation, challenge and new application in sensors of its film electrode: a review. J Polym Sci A Polym Chem. 2017;55(7):1121–50.
59. Hiwrale A, Bharati S, Pingale P, Rajput A. Nanofibers: a current era in drug delivery system. Heliyon. 2023. https://doi.org/10.1016/j.heliyon.2023.e18917.
60. Balusamy B, Celebioglu A, Senthamizhan A, Uyar T. Progress in the design and development of fast-dissolving electrospun nanofibers based drug delivery systems-a systematic review. J Controlled Release. 2020;326:482–509.
61. Shastri SS, Varma P, Kandasubramanian B. Enhancing drug delivery with electrospun biopolymer nanofibers. Biomedical Mater Devices. 2024:1–24.
62. Zhang T, Xu H, Zhang Y, Zhang S, Yang X, Wei Y, et al. Fabrication and characterization of double-layer asymmetric dressing through electrostatic spinning and 3D printing for skin wound repair. Mater Design. 2022;218:110711.
63. Sharma D, Saha D, Satapathy BK. Structurally optimized suture resistant polylactic acid (PLA)/poly (ε-caprolactone)(PCL) blend based engineered nanofibrous mats. J Mech Behav Biomed Mater. 2021;116:104331.
64. Wen N, Zhang L, Jiang D, Wu Z, Li B, Sun C, et al. Emerging flexible sensors based on nanomaterials: recent status and applications. J Mater Chem A. 2020;8(48):25499–527.
65. Cheng M, Zhu G, Zhang F, Tang W-l, Jianping S, Yang J-q, et al. A review of flexible force sensors for human health monitoring. J Adv Res. 2020;26:53–68.
66. Wang Z, Cong Y, Fu J. Stretchable and tough conductive hydrogels for flexible pressure and strain sensors. J Mater Chem B. 2020;8(16):3437–59.
67. Feng F, Zhao Z, Li J, Huang Y, Chen W. Multifunctional dressings for wound exudate management. Prog Mater Sci. 2024. https://doi.org/10.1016/j.pmatsci.2024.101328.
68. Pooresmaeil M, Namazi H. Facile preparation of pH-sensitive chitosan microspheres for delivery of curcumin; characterization, drug release kinetics and evaluation of anticancer activity. Int J Biol Macromol. 2020;162:501–11.
69. Ramadon D, McCrudden MT, Courtenay AJ, Donnelly RF. Enhancement strategies for transdermal drug delivery systems: current trends and applications. Drug Delivery Translational Res. 2021:1–34.
70. Ren K, Cheng Y, Huang C, Chen R, Wang Z, Wei J. Self-healing conductive hydrogels based on alginate, gelatin and polypyrrole serve as a repairable circuit and a mechanical sensor. J Mater Chem B. 2019;7(37):5704–12.
71. Rogers ZJ, Zeevi MP, Koppes R, Bencherif SA. Electroconductive hydrogels for tissue engineering: current status and future perspectives. Bioelectricity. 2020;2(3):279–92.
72. Wallace LA, Gwynne L, Jenkins T. Challenges and opportunities of pH in chronic wounds. Ther Deliv. 2019;10(11):719–35.
73. Motasadizadeh H, Azizi S, Shaabani A, Sarvestani MG, Sedghi R, Dinarvand R. Development of PVA/chitosan-g-poly (N-vinyl imidazole)/TiO2/curcumin nanofibers as high-performance wound dressing. Carbohydr Polym. 2022;296:119956.
74. Aytac Z, Uyar T. Core-shell nanofibers of curcumin/cyclodextrin inclusion complex and polylactic acid: enhanced water solubility and slow release of curcumin. Int J Pharm. 2017;518(1–2):177–84.
75. Ahmad Ruzaidi DA, Mahat MM, Mohamed Sofian Z, Nor Hashim NA, Osman H, Nawawi MA, et al. Synthesis and characterization of porous, electro-conductive chitosan–gelatin–agar-based PEDOT: PSS scaffolds for potential use in tissue engineering. Polymers. 2021;13(17):2901.
76. Wan F, Hu K, Liu R, Zhang S, Li S, Lei Y, et al. Ice-template-induced highly ionic conductive PVA/PEG-SiO 2 gel polymer electrolyte for zinc-ion batteries. Chem Commun. 2024;60(56):7220–3.
77. Rauer SB, Bell DJ, Jain P, Rahimi K, Felder D, Linkhorst J, et al. Porous PEDOT: PSS particles and their application as tunable cell culture substrate. Adv Mater Technol. 2022;7(1):2100836.
78. Furlani F, Campodoni E, Sangiorgi N, Montesi M, Sanson A, Sandri M, et al. Electroconductive scaffolds based on gelatin and PEDOT: PSS for cardiac regeneration. Int J Biol Macromol. 2023;224:266–80.
79. Bayrakci M, Keskinates M, Yilmaz B. Antibacterial, thermal decomposition and in vitro time release studies of chloramphenicol from novel PLA and PVA nanofiber mats. Mater Sci Eng C Mater Biol Appl. 2021;122:111895.
80. Shefa AA, Sultana T, Park MK, Lee SY, Gwon J-G, Lee B-T. Curcumin incorporation into an oxidized cellulose nanofiber-polyvinyl alcohol hydrogel system promotes wound healing. Mater Des. 2020;186:108313.
81. Asadi N, Del Bakhshayesh AR, Davaran S, Akbarzadeh A. Common biocompatible polymeric materials for tissue engineering and regenerative medicine. Mater Chem Phys. 2020;242:122528.
82. Yao L, Yao L, Li Y. Electric Field-Guided Cell Migration, Polarization, and Division: An Emerging Therapy in Neural Regeneration. In: Glial Cell Engineering in Neural Regeneration. 2018. p. 85–109.
83. Zhu K, Takada Y, Nakajima K, Sun Y, Jiang J, Zhang Y, et al. Expression of integrins to control migration direction of electrotaxis. FASEB J. 2019;33(8):9131.
84. Ko UH, Choi J, Choung J, Moon S, Shin JH. Physicochemically tuned myofibroblasts for wound healing strategy. Sci Rep. 2019;9(1):16070.
85. Ho M, Thompson B, Fisk JN, Nebert DW, Bruford EA, Vasiliou V, et al. Update of the keratin gene family: evolution, tissue-specific expression patterns, and relevance to clinical disorders. Hum Genomics. 2022;16:1–21.
86. Cohen E, Johnson C, Redmond CJ, Nair RR, Coulombe PA. Revisiting the significance of keratin expression in complex epithelia. J Cell Sci. 2022;135(20):jcs260594.
87. Terada CI, Onoue K, Fujii T, Itami H, Morita K, Uchiyama T, et al. Histopathological and epigenetic changes in myocardium associated with cancer therapy-related cardiac dysfunction. ESC Heart Fail. 2022;9(5):3031–43.
88. Rajkumar J, Chandan N, Lio P, Shi V. The skin barrier and moisturization: function, disruption, and mechanisms of repair. Skin Pharmacol Physiol. 2023;36(4):174–85.
89. Ding C, Liu X, Zhang S, Sun S, Yang J, Chai G, et al. Multifunctional hydrogel bioscaffolds based on polysaccharide to promote wound healing: a review. Int J Biol Macromol. 2024. https://doi.org/10.1016/j.ijbiomac.2024.129356.
90. Sun X, Yang Y, Yu J, Wei Q, Ren X. Chitosan-based supramolecular aerogel with "skeletal structure" constructed in natural deep eutectic solvents for medical dressings. Int J Biol Macromol. 2024;254:127720.

91. Wang Z, Hu W, Wang W, Xiao Y, Chen Y, Wang X. Antibacterial electrospun nanofibrous materials for wound healing. Adv Fiber Mater. 2023;5(1):107–29.
92. Mireshghi N, Jafari Z. Comparison of the effect of nano Curcumin on the expression of some drug resistance genes in Gram-negative and Gram-positive bacteria. Journal of Medicinal plants and By-Products; 2024.
93. Mendes SG, Combo SI, Allain T, Domingues S, Buret AG, Da Silva GJ. Co-regulation of biofilm formation and antimicrobial resistance in *acinetobacter baumannii*: from mechanisms to therapeutic strategies. Eur J Clin Microbiol Infect Dis. 2023;42(12):1405–23.
94. Girardeau-Hubert S, Lynch B, Zuttion F, Label R, Rayee C, Brizion S, et al. Impact of microstructure on cell behavior and tissue mechanics in collagen and dermal decellularized extra-cellular matrices. Acta Biomater. 2022;143:100–14.
95. Hadi MF, Barocas VH. Microscale fiber network alignment affects macroscale failure behavior in simulated collagen tissue analogs. J Biomech Eng. 2013;135(2):021026.
96. Du S, Zhou N, Xie G, Chen Y, Suo H, Xu J, et al. Surface-engineered triboelectric nanogenerator patches with drug loading and electrical stimulation capabilities: toward promoting infected wounds healing. Nano Energy. 2021;85:106004.
97. Zhang J, Neoh KG, Hu X, Kang E-T. Mechanistic insights into response of *Staphylococcus aureus* to bioelectric effect on polypyrrole/chitosan film. Biomaterials. 2014;35(27):7690–8.
98. Fang G, Wang J, Yang Q, Li M, Huang H. Highly-efficient cathodic lysis of biofilm on conductive carbon nanotube membranes. Sep Purif Technol. 2023;304:122327.
99. Li R, Xiang H, Liang Q, Zhou Y, Ma X, Chao D, et al. Engineering the electrochemistry of a therapeutic Zn battery toward biofilm microenvironment for diabetic wound healing. Nano Energy. 2024;128:109946.

Publisher's note